Chapter 2 – SHOCK INTERACTIONS AND CONTROL SURFACES

Doyle Knight
Rutgers University
USA

Jose Longo
ESTEC
NETHERLANDS

2.1 INTRODUCTION

Renewed interest in hypersonic air vehicles such as the Boeing X-51 (Figure 2-1) has focused research on topics critical to hypersonic flight. The design of hypersonic air vehicles involves numerous engineering disciplines including aerothermodynamic analysis. In particular, the interaction of shock waves with the vehicle boundary layers can lead to regions of enhanced aerothermodynamic loading, and therefore accurate modeling of shock wave boundary layer interaction ("shock interactions") is essential.

Figure 2-1: Boeing X-51 Waverider.

During the past decade two NATO Research Technology Organisation (RTO) Working Groups (WGs) have assessed the capabilities for prediction of aerothermodynamic loads in high speed flight. AGARD Working Group 18 (WG18) examined the Computational Fluid Dynamics (CFD) capability for prediction of 2-D and 3-D perfect gas shock wave laminar and turbulent boundary layer interactions for three generic configurations: single fin (Figure 2-2), double fin (Figure 2-3) and hollow cylinder flare (Figure 2-4) [12]. The single and double fin configurations involved shock wave turbulent boundary layer interactions, while the hollow cylinder configuration included both laminar and turbulent shock boundary layer interactions. All cases were perfect gas flows. All turbulent flow simulations were performed using Reynolds-Averaged Navier-Stokes (RANS) models. The report concluded that laminar perfect gas shock interactions were accurately predicted. The report concluded that while turbulent perfect gas shock interaction predictions were accurate for 3-D mean pressure and primary separation locations, nevertheless the skin friction and heat transfer were poorly predicted.

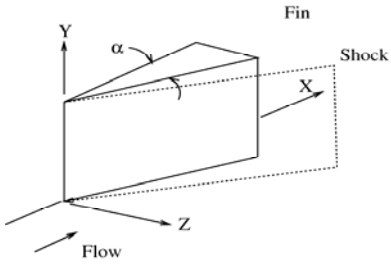

Figure 2-2: Single Fin.

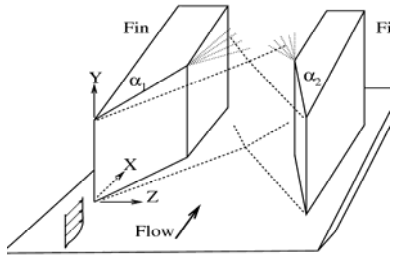

Figure 2-3: Double Fin.

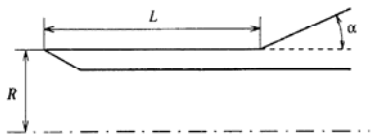

Figure 2-4: Hollow Cylinder.

RTO Working Group 10 (WG10) conducted a detailed examination of CFD capability for six areas relevant to hypersonic flight: boundary layer instability and transition, real gas flows, laminar hypersonic viscous-inviscid interactions, shock-shock interactions, shock wave-turbulent boundary layer interactions and base flows with and without plume interaction [13]. Sub-Group 3 of WG10 examined CFD capability for shock wave-turbulent boundary layer interactions focusing on five generic configurations: 2-D compression corner (Figure 2-5), 2-D compression-expansion corner (Figure 2-6), 2-D shock impingement (Figure 2-7), 3-D single fin (Figure 2-2) and 3-D double fin (Figure 2-3). All cases were perfect gas flows. All 2-D shock interaction flow simulations were performed using either Direct Numerical Simulation (DNS) or Large Eddy Simulation (LES) models, and all 3-D shock interaction flow simulations were performed using RANS methods. The report concluded that DNS and LES results for 2-D shock wave turbulent boundary layer interactions showed significant progress in predicting the flow; however, the Reynolds numbers of the simulations were relatively low due to computational resource requirements, and no comparison with experimental surface heat transfer measurements was performed. The report concluded that new RANS concepts for 3-D shock wave turbulent boundary layer interactions showed improvement in prediction of the flow; however, heat transfer was not accurately predicted.

Figure 2-5: Compression Corner.

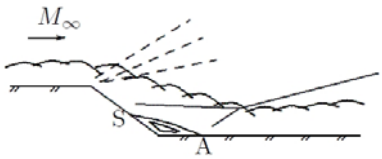

Figure 2-6: Compression-Expansion.

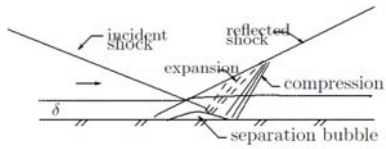

Figure 2-7: Shock Impingement.

RTO AVT Task Group 43 Topic No. 2 focuses on a further assessment of CFD for the specific issue of shock interactions and control surfaces in non-equilibrium flows. This report presents a comparison of computed and experimental results for two new configurations. The first configuration is a double cone (Figure 2-8) from CUBRC. The second configuration is a cylinder (Figure 2-9) from DLR. Experimental surface pressure and heat transfer data are available for two different enthalpy conditions under laminar flow conditions for each configuration, and constitute the primary measures for assessing the accuracy of the CFD simulations.

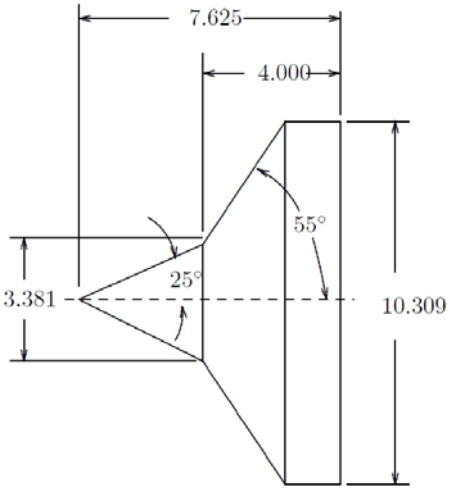

Figure 2-8: Double Cone.

Figure 2-9: Cylinder.

2.2 EXPERIMENTS

2.2.1 Double Cone

The experiments were conducted in the LENS I shock tunnel at CUBRC to obtain detailed surface and flow characteristics over a double cone configuration with semi angles of 25° and 55° and a base diameter of 10.3 inches (Figure 2-8). Measurements were made in nitrogen for total enthalpy conditions of 5.38 and 9.17 MJ/kg creating conditions with negligible dissociation. In allied studies, measurements were made to determine the velocity and NO concentration in the freestream for the airflows. The measured freestream velocity was in excellent agreement with non-equilibrium flow predictions using the nozzle code of Candler [3]. However, the measured NO concentration was measurably less than the predicted levels. The test conditions are shown in Table 2-1 where subscripts $_o$ and $_\infty$ represent reservoir and test section conditions, respectively. The values represent best estimates based on measurements made in the reservoir and freestream in flow calibration studies.

Table 2-1: Test Conditions for Double Cone.

Quantity	*Run 40*	*Run 42*	*Quantity*	*Run 40*	*Run 42*
h_o (MJ/kg)	5.38	9.17	T_∞ (K)	173	303
p_o (MPa)	17.3	17.9	$T_{\infty, vib}$ (K)	2735	3085
T_o (K)	4327	6611	$c[N_2]$	1.0000	0.9973
U_∞ (m/s)	3094	4065	$c[O_2]$	0.0000	0.0000
p_∞ (Pa)	129	121	$c[NO]$	0.0000	0.0000
ρ_∞ (kg/m^3)	$2.52 \cdot 10^{-3}$	$1.34 \cdot 10^{-3}$	$c[N]$	0.0000	0.0027
			$c[O]$	0.0000	0.0000

2.2.2 Cylinder

A test campaign [11] to investigate the flow past a cylindrical model was performed at the high enthalpy shock tunnel (HEG) of the German Aerospace Center (DLR). The cylindrical model, with a radius of 45 mm and a span of 380 mm, was mounted on the nozzle centerline with its axis transverse to the flow. It was equipped with 17 pressure transducers and the same number of thermocouples to measure surface pressure and heat flux distributions. The transducers were distributed along six rows located close to the plane of symmetry at the mid-span location (10, 20 and 30 mm to the left and right of the plane of symmetry, covering a circumferential angle of 60° with respect to the inflow direction).

The large shock stand-off distance of this configuration permits the application of optical measurement techniques for the determination of the gas properties in the shock layer. Holographic interferometry and time resolved Schlieren were applied to measure density distributions in the shock layer and the temporal evolution of the bow shock shape. Free stream static and Pitot pressures and stagnation heat transfer on a sphere were recorded at each run for calibration, normalization and statistical purposes.

The measurements on the cylinder were carried out at different total enthalpies (HEG conditions I and III, 22.4 MJ/kg and 13.5 MJ/kg, respectively) and with air as a test gas. The HEG reservoir and free stream data for the measurements are listed in Table 2-2.

Table 2-2: Test Conditions for Cylinder.

Quantity	*I*	*III*	*Quantity*	*I*	*III*
h_o (MJ/kg)	22.4	13.5	$p_{p\infty}$ (kPa)	52.9	70.8
p_o (MPa)	35.0	48.3	M_∞	8.98	8.78
T_o (K)	9200	7370	$c[N_2]$	0.7543	0.7356
U_∞ (m/s)	5956	4776	$c[O_2]$	0.00713	0.1340
p_∞ (Pa)	476	687	$c[NO]$	0.01026	0.0509
ρ_∞ (kg/m^3)	$1.547 \cdot 10^{-3}$	$3.26 \cdot 10^{-3}$	$c[N]$	$6.5 \cdot 10^{-7}$	0.0000
T_∞ (K)	901	694	$c[O]$	0.2283	0.07955

At the experimental conditions the flow in the shock layer is subject to non-equilibrium chemical relaxation processes that significantly affect the density distribution and hence the shock stand-off distance. Therefore, this test case represents a useful basis for the validation of the physico-chemical models used in CFD codes.

2.3 PARTICIPANTS

Computations of the double cone and cylinder were solicited from experts in the US and Europe. The participants are listed in Table 2-3. All aspects of the computations were determined individually by the participants including the selection of thermochemistry model, numerical algorithm, grid refinement study and convergence criteria. Details of the computations are presented in Section 2.4 organized by participant.

Table 2-3: Participants.

Name	*Organization*
Datta Gaitonde	Air Force Research Labs, Wright-Patterson AFB, OH, USA
Andrea Lani	Von Karman Institute for Fluid Dynamics, Brussels, Belgium
Dimitris Drikakis, Andrew Mosedale	Cranfield University, Cranfield, United Kingdom
Ioannis Nompelis	Dept Aerospace Engineering and Mechanics, Univ. of Minnesota, MN, USA
Bodo Reimann	German Aerospace Center (DLR), Braunschweig, Germany
Louis Walpot	Advanced Operations and Engineering Services, Netherlands

2.4 COMPUTATIONAL METHODS

2.4.1 Datta Gaitonde

All results were obtained with the GASP code. For the double cone cases, two grids were computed. The inviscid terms are discretized with the Roe scheme [26], extended to include high-temperature effects [21], and combined with the third-order upwind-biased MUSCL approach and the van Albada limiter. Viscous terms were computed in a centered fashion. The solution was marched in time with an implicit dual-stepping time-accurate algorithm. The simulation assumes fully catalytic walls with the Park I model which considers vibrational relaxation but neglects ionization [24]. Radiation has been ignored in all calculations.

For the cylinder cases, the flow was simulated in both 3-D and 2-D (centerplane) but assuming horizontal symmetry. The 3-D slice corresponding to the spanwise center of the cylinder shows essentially the same result as the 2-D computation. The inviscid terms are discretized with the AUSM+ method [17] combined with the third-order upwind-biased MUSCL approach and the minmod limiter. Viscous terms were computed in a centered fashion. The solution was marched in time with an implicit dual-stepping time-accurate algorithm. The simulation assumes fully catalytic walls with the Park I model which considers vibrational relaxation but neglects ionization [24]. Radiation has been ignored in all calculations.

2.4.2 Andrea Lani

The double cone Run 40 and Cylinder (I and III) test cases were computed with a parallel implicit cell-centered Finite Volume solver for unstructured meshes [16] implemented within the COOLFluiD collaborative software environment [14], [15], [16], [27]. In particular, we have used a modified AUSM+ scheme [16], [17] in combination with a multi-dimensional weighted least square reconstruction [1] and Venkatakhrisnan's limiter [29]. The results for double cone Run 42 have been computed with a parallel implicit vertex-centered Conservative Residual Distribution solver [4], [16] again implemented in COOLFluiD [16]. In particular, the second order accurate blended Bxc scheme has been employed [5]. In Runs 40 and 42, the flow is modeled as a neutral nitrogen mixture (N_2-N) in thermo-chemical non-equilibrium with a two temperature model. The corresponding reaction rate coefficients are given in Nompelis [22]. A three temperature model (including roto-translational T, vibrational temperatures of N_2 and O_2) has been applied to the cylinder test cases. In this case, the flow is treated as a five species air mixture with reaction rate coefficients given by Park [25]. More details about the modeling of transport, thermodynamics, chemistry and energy relaxation can be found in [16], [19] and [23].

2.4.3 Dimitris Drikakis, Andrew Mosedale

The computations at Cranfield University were performed using the code CNS3D [6], [7], [8]. The code comprises a library of numerical methods, including second- and fifth-order MUSCL schemes with low-Mach corrections and very high-order WENO schemes up to ninth-order accurate, for spatial discretization. The time integration is obtained by TVD Runge-Kutta schemes, third- and fifth-order accurate. The code can be used for Unsteady Reynolds-Averaged Navier-Stokes (URANS) and Implicit Large Eddy Simulations (ILES). CNS3D is fully parallelized using MPI systems and has been ported onto several high-performance computing facilities including Cranfield's 7.8 Tflops machine and the United Kingdom's national HPCx among others. The code employs the two temperature model by Park for non-equilibrium thermochemistry assuming that the translational and rotational modes of energy as well as the vibrational and electronic modes of energy are in equilibrium. Other capabilities of the code include ablation modeling, coupling of solid and fluid mechanics as well as coupling of molecular dynamics with CFD.

2.4.4 Ioannis Nompelis

The Navier-Stokes equations with chemistry are solved for a mixture of perfect gases that is in non-equilibrium. We solve a separate conservation equation for each of the five species and Park's rates are used as well as Park's TTv model for vibration-dissociation coupling [24]. A separate vibrational energy equation for the mixture is solved together with the momentum and total energy equations. A Simple Harmonic Oscilator (SHO) model is used, assuming that all vibrational models are in equilibrium. The Landau-Teller model [30] with Millikan and White [20] rates is employed for energy relaxation. The equations are solved with a finite volume code that uses the modified Steger-Warming flux splitting [18]. To achieve second order spatial accuracy a MUSCL [9] extrapolation is done to the primative variables. The viscous fluxes are evaluated with a finite difference form and viscosity coefficients are calculated from Blottner fits [2] with Wilke's mixing rule for the mixture. The equations are integrated with a fully implicit line-relaxation method [31].

2.4.5 Bodo Reimann

The flow solver is the DLR TAU code [28]. The Reynolds-averaged Navier-Stokes equations are discretized by a finite volume scheme. The AUSMDV second order upwind scheme with MUSCL reconstruction is used for the inviscid fluxes. For time discretization, local and dual time stepping, with a three-stage Runge-Kutta method, as well as an implicit, approximately factored LU-SGS scheme have been used. For acceleration, multi-grid and explicit residual smoothing are available. Furthermore, parallel computing is possible via domain splitting and Message Passing Interface (MPI) communication. To model the thermochemical behavior of the flow, the Gupta et al. [10] five species chemical non-equilibrium model was applied to the cylinder case. For the double cone case, the reaction rates for nitrogen given by Park [25] have been used. Thermal non-equilibrium is accounted for by a two temperature model according to Park. The relaxation of the vibrational energy of the nitrogen molecules is described by a Landau-Teller formulation using the Millikan-White relaxation times. The structured cylinder grid has 49 x 93 x 121 grid points. The grid is refined at the location where the shock is expected. For the double cone the fine mesh with 1024 x 513 grid points given by Nompelis is used.

2.4.6 Louis Walpot

The full unsteady laminar Navier-Stokes equations are solved using a finite volume algorithm. The double cone computations assume a two species (N_2 and N) mixture, and the cylinder computations assume a five species (N_2, O_2, NO, N, O) mixture. Viscosity is specified using Wilke's Mixing Rule. A two temperature thermochemistry model is utilized. The algorithm is second order accurate. Van Albada limiter is used.

2.5 RESULTS

2.5.1 Flowfield Structure

The structure of the double cone flowfield for the cases considered is illustrated in Figure 2-10. The first cone generates an incident shock wave which is close to the cone surface. The incident shock interacts with the shock wave generated by the second cone to form a shock-shock interaction. The impingement of the incident shock upon the cone surface causes a rapid pressure rise and concommitant separation. A recirculation region forms with separation and reattachment points. The increase in displacement thickness caused by the separation region induces the formation of a separate separation shock. The separation point is indicated in the experiment by a rapid decrease in heat transfer, and similarly the reattachment point is identified by a rapid increase in heat transfer. The separation region is identified by a plateau in surface pressure.

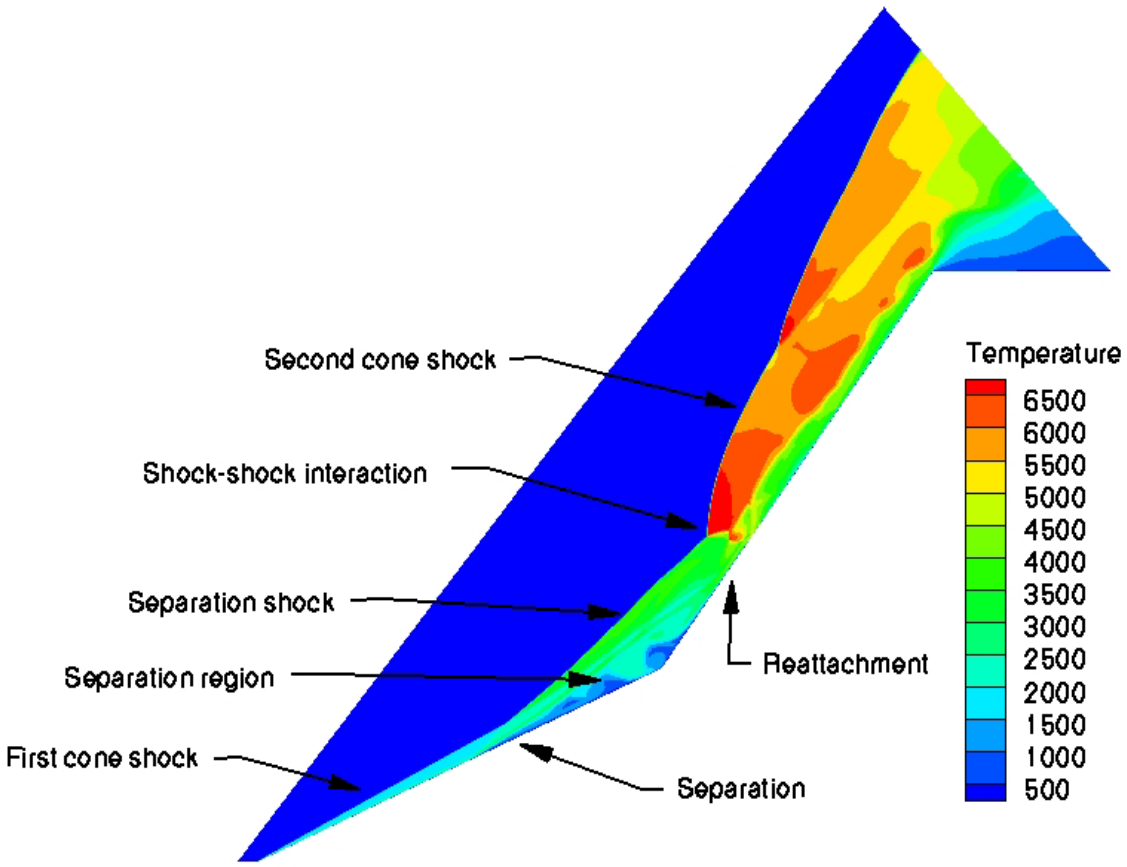

Figure 2-10: Double Cone Flowfield Structure (from Gaitonde).

The structure of the cylinder flowfield in the symmetry (center) plane is illustrated in Figure 2-11. The blunt body shock wave and streamlines are indicated. The stagnation point corresponds to the maximum surface pressure and heat transfer. The flow in the shock layer experiences significant non-equilibrium chemical and thermal relaxation processes which influences the shock stand-off distance.

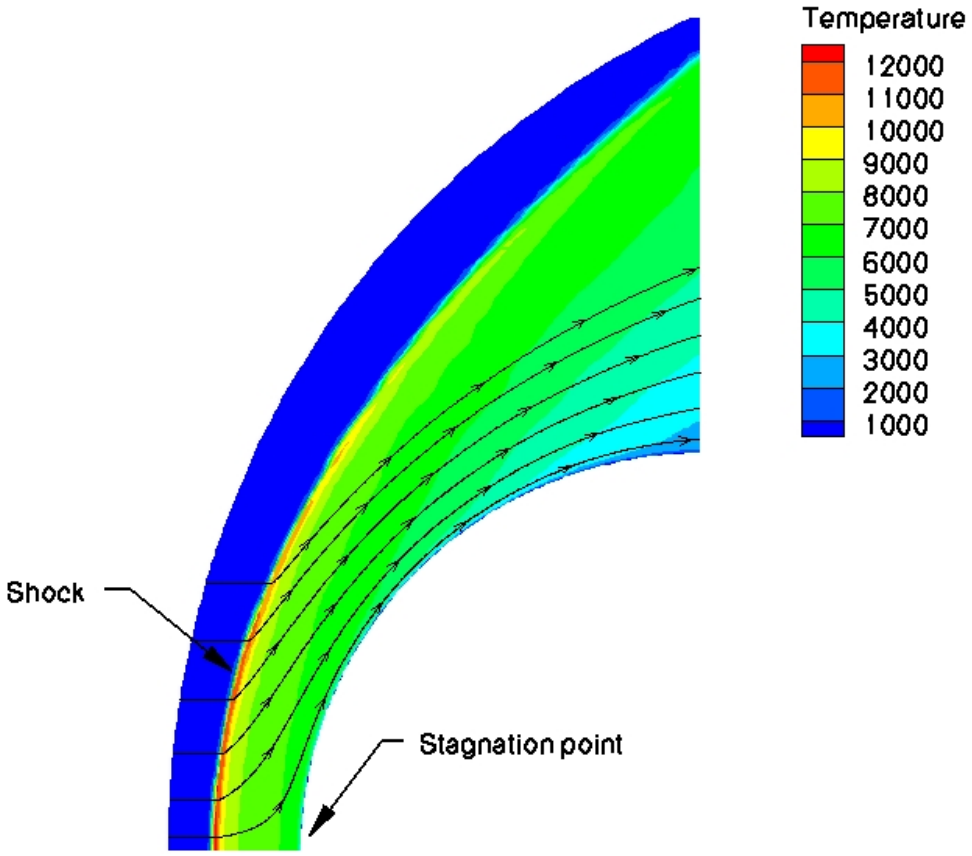

Figure 2-11: Cylinder Flowfield Structure (from Gaitonde).

2.5.2 Double Cone

2.5.2.1 Run 40

The computed surface pressure is compared with experiment in Figure 2-12 to Figure 2-17. The results of Gaitonde (Figure 2-12), Nompelis (Figure 2-15) and Walpot (Figure 2-17) indicate strong unsteadiness in the flowfield with a strongly unsteady separation region at the corner. Gaitonde, Nompelis and Walpot observed that their computations did not achieve steady state. The results of Lani (Figure 2-13), Drikakis et al. (Figure 2-14) and Reimann (Figure 2-16) are instantaneous “snapshots” of the surface pressure. In private communication, all three indicated that the computed flowfield was unsteady and did not achieve a steady state. The computed surface heat transfer is compared with experiment in Figure 2-18 to Figure 2-23. The results of Gaitonde (Figure 2-18), Nompelis (Figure 2-21) and Walpot (Figure 2-23) show similar unsteadiness as expected from the surface pressure computations. The results of Lani (Figure 2-19), Drikakis et al. (Figure 2-20) and Reimann (Figure 2-22) are instantaneous “snapshots” as previous.

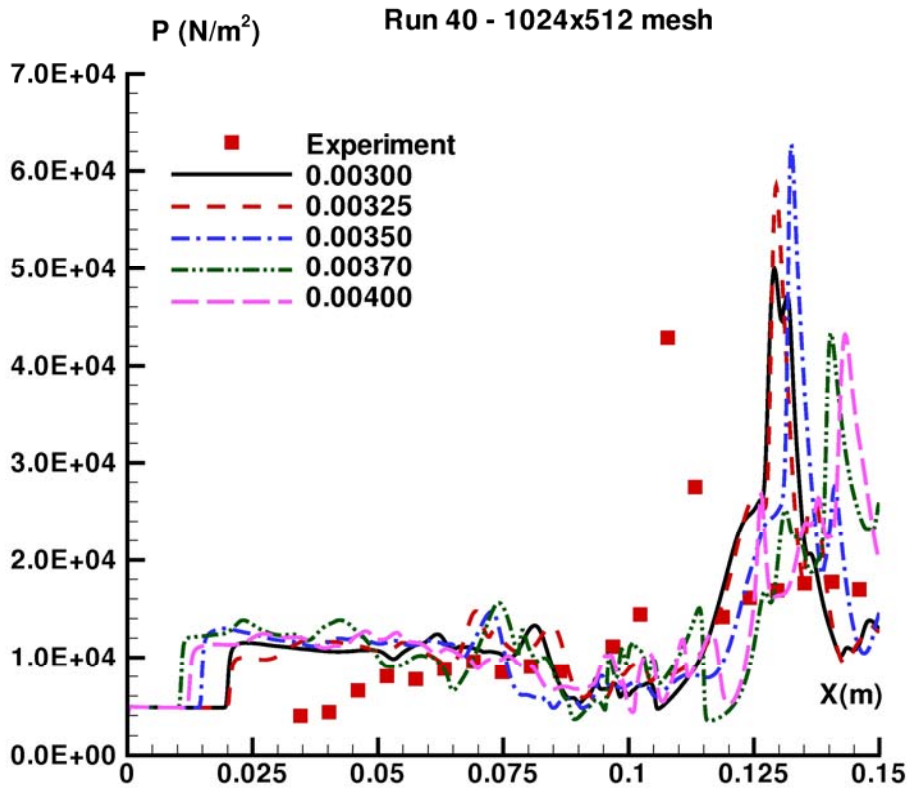

Figure 2-12: p_w for Run 40 (Gaitonde) [Time counter is notional and does not represent absolute time].

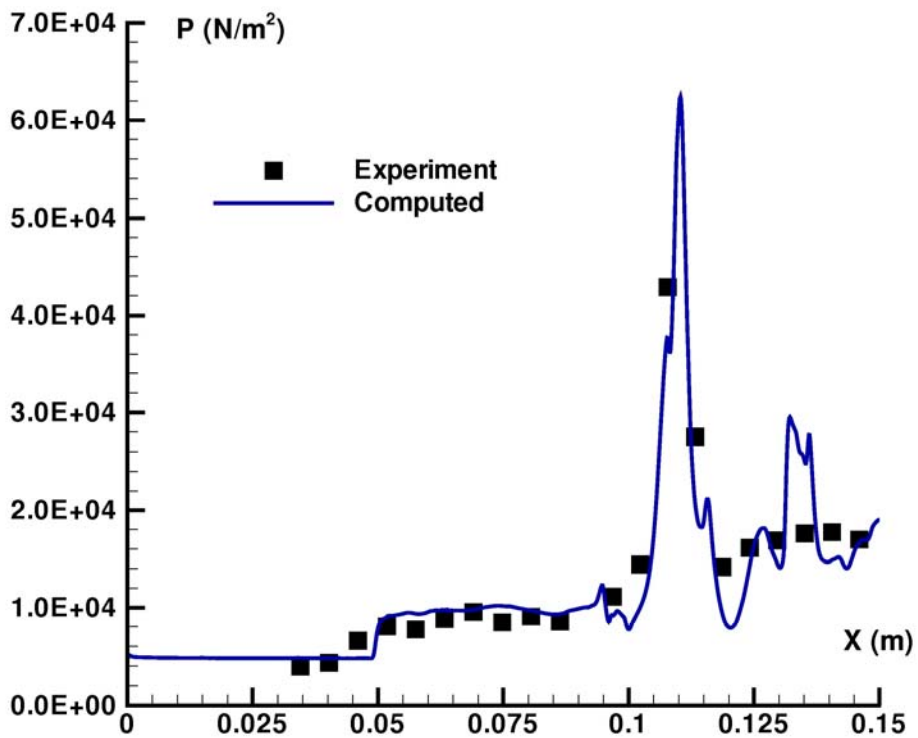

Figure 2-13: p_w for Run 40 (Lani).

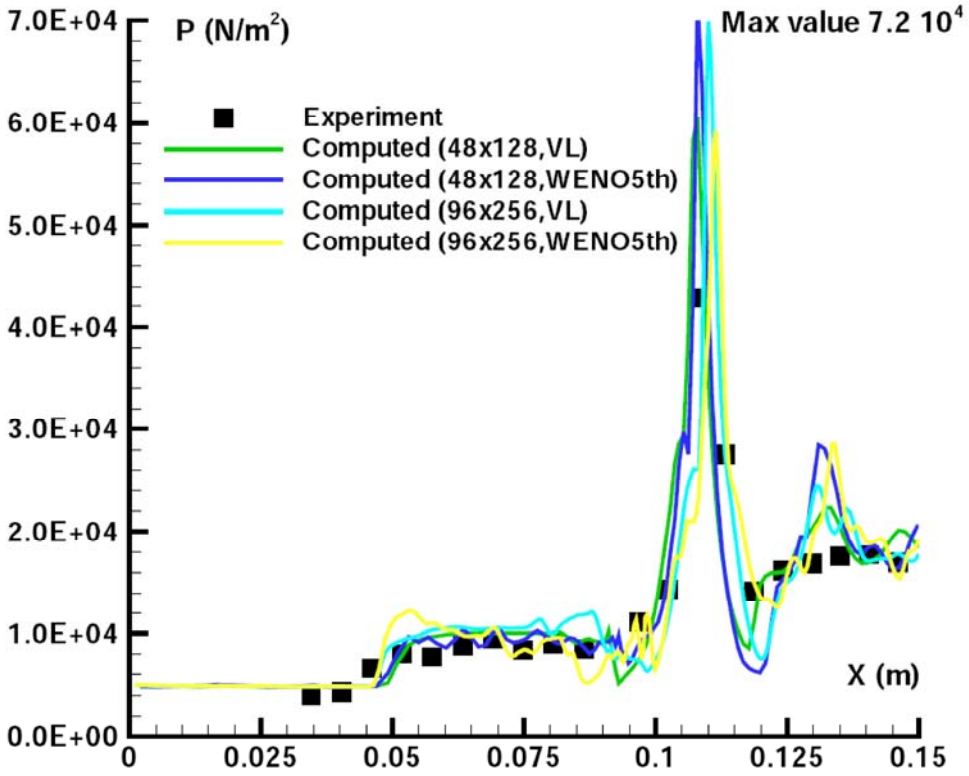

Figure 2-14: p_w for Run 40 (Drikakis et al.).

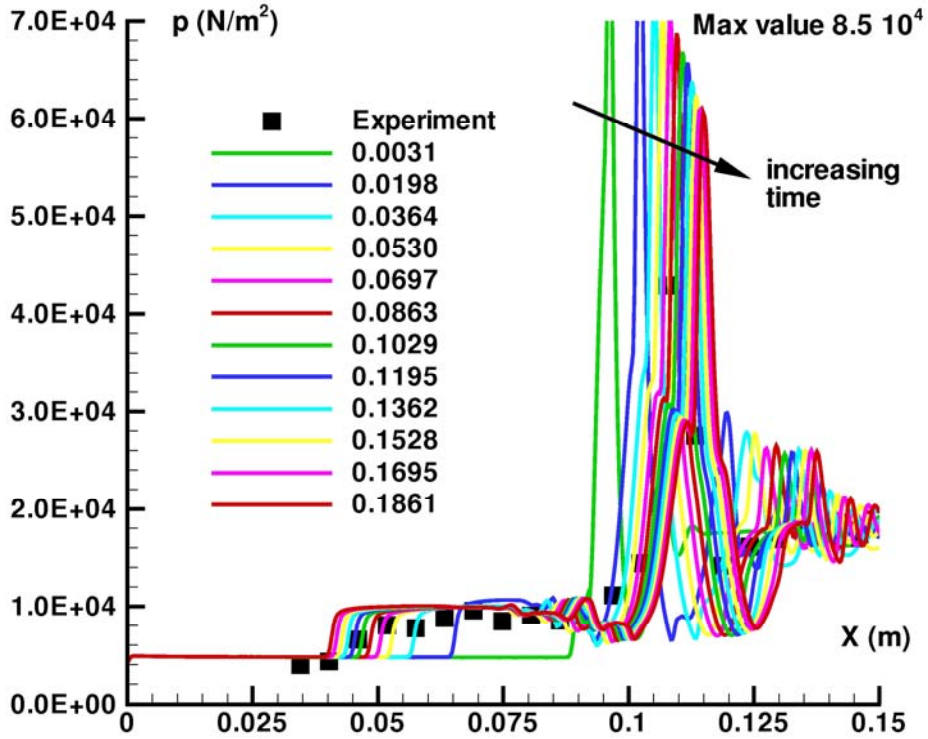

Figure 2-15: p_w for Run 40 (Nompelis).

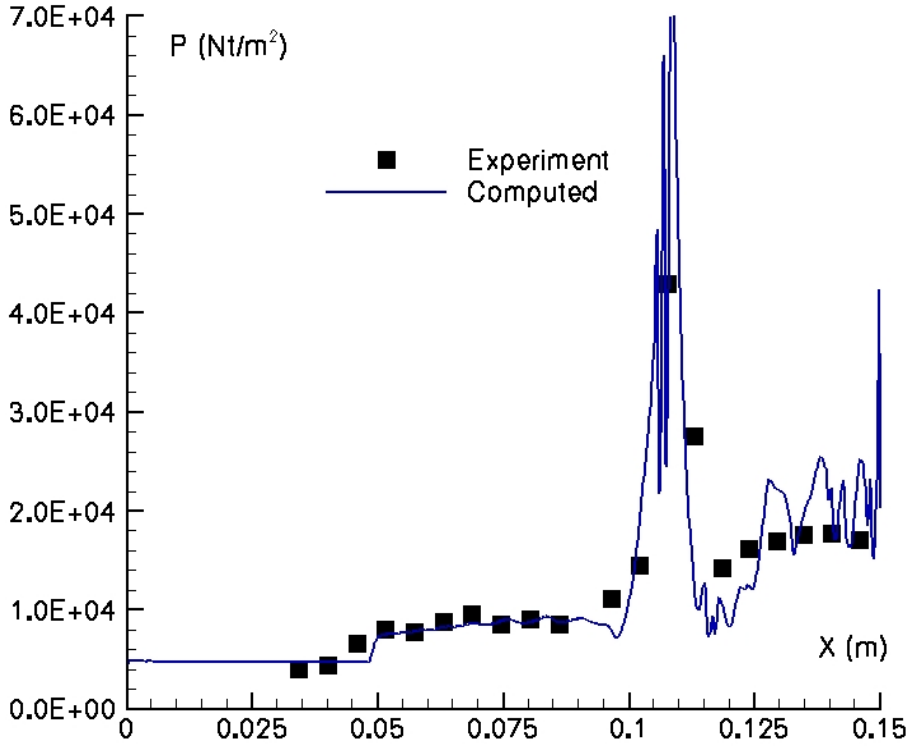

Figure 2-16: p_w for Run 40 (Reimann).

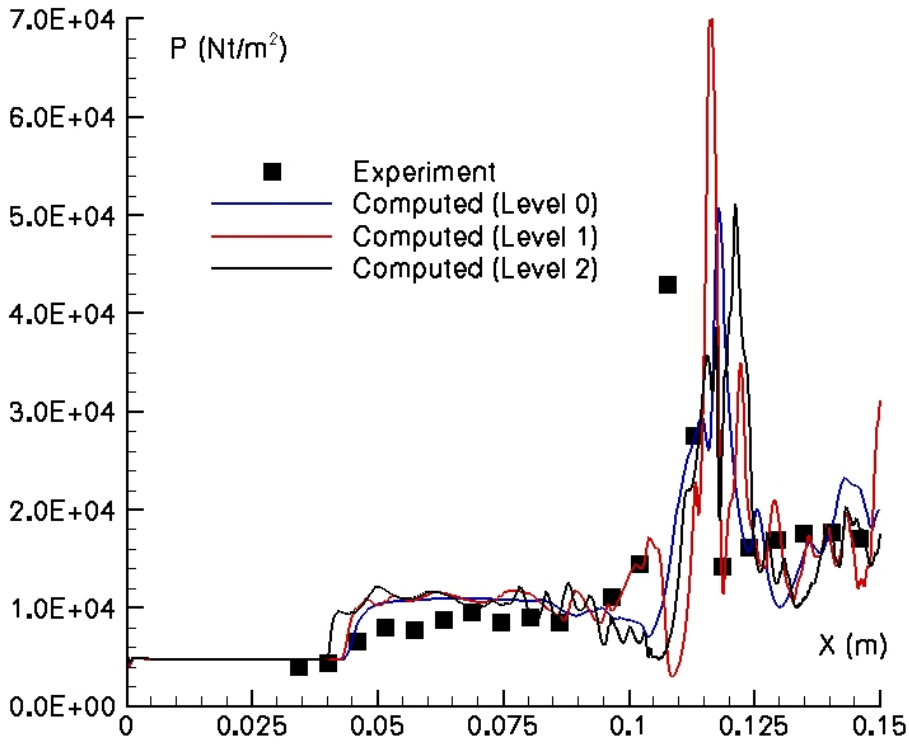

Figure 2-17: p_w for Run 40 (Walpot).

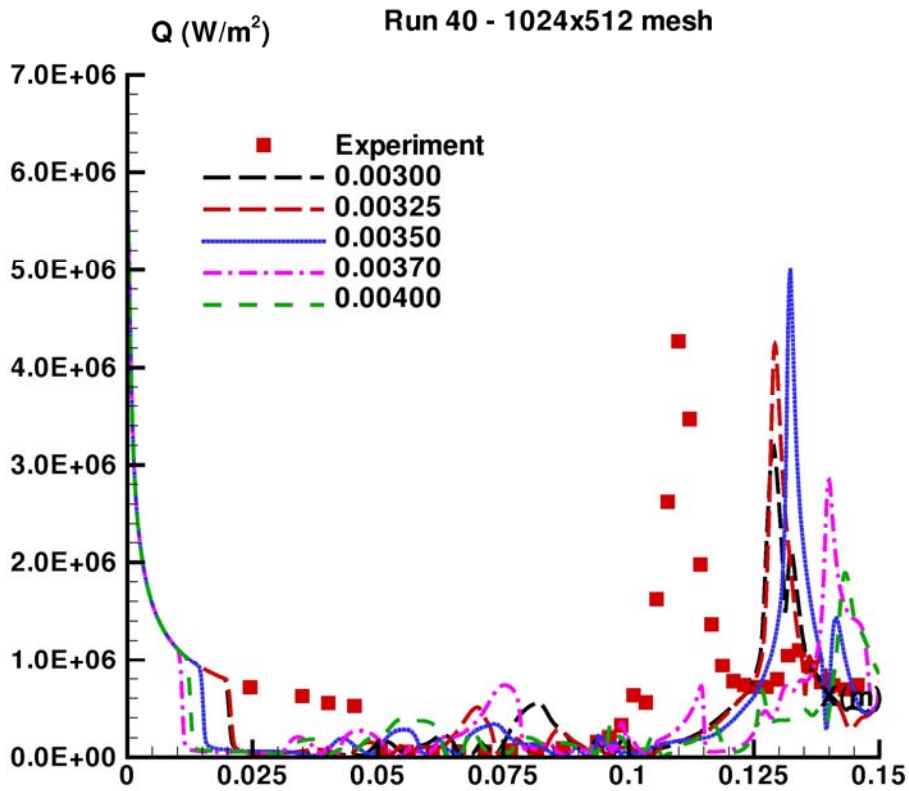

Figure 2-18: q_w for Run 40 (Gaitonde) [Time counter is notional and does not represent absolute time].

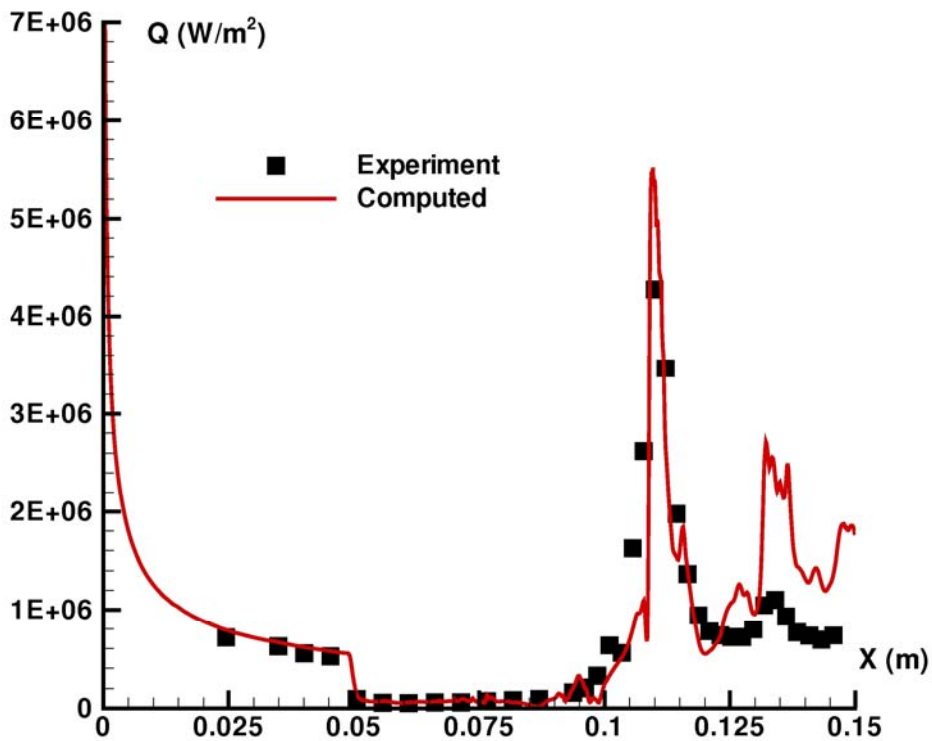

Figure 2-19: q_w for Run 40 (Lani).

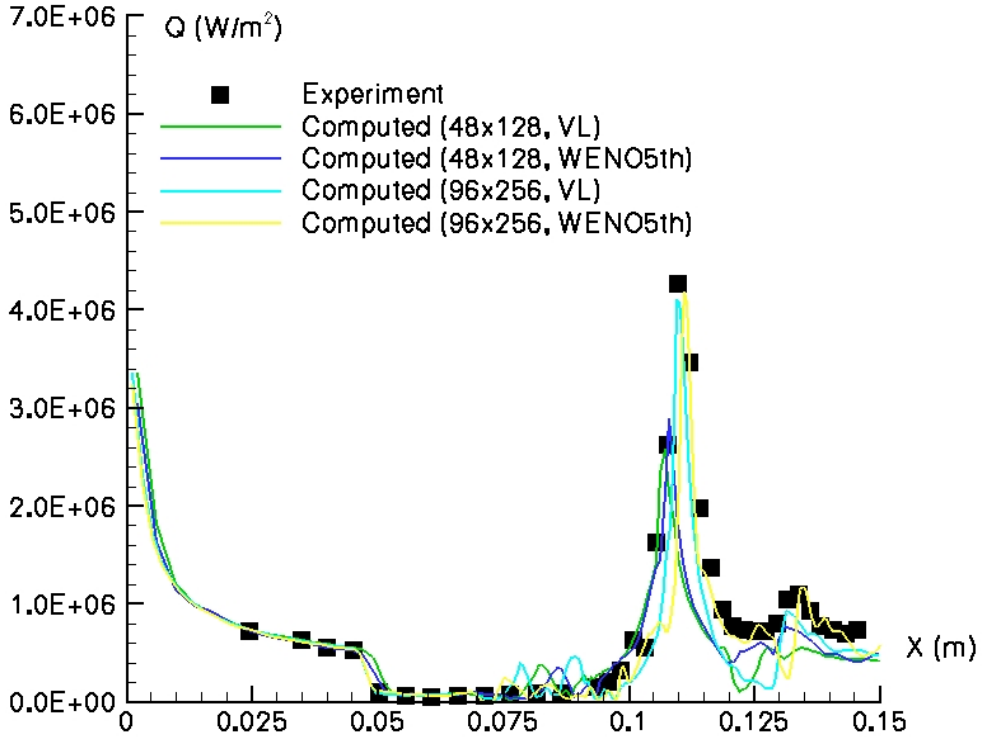

Figure 2-20: q_w for Run 40 (Drikakis et al.).

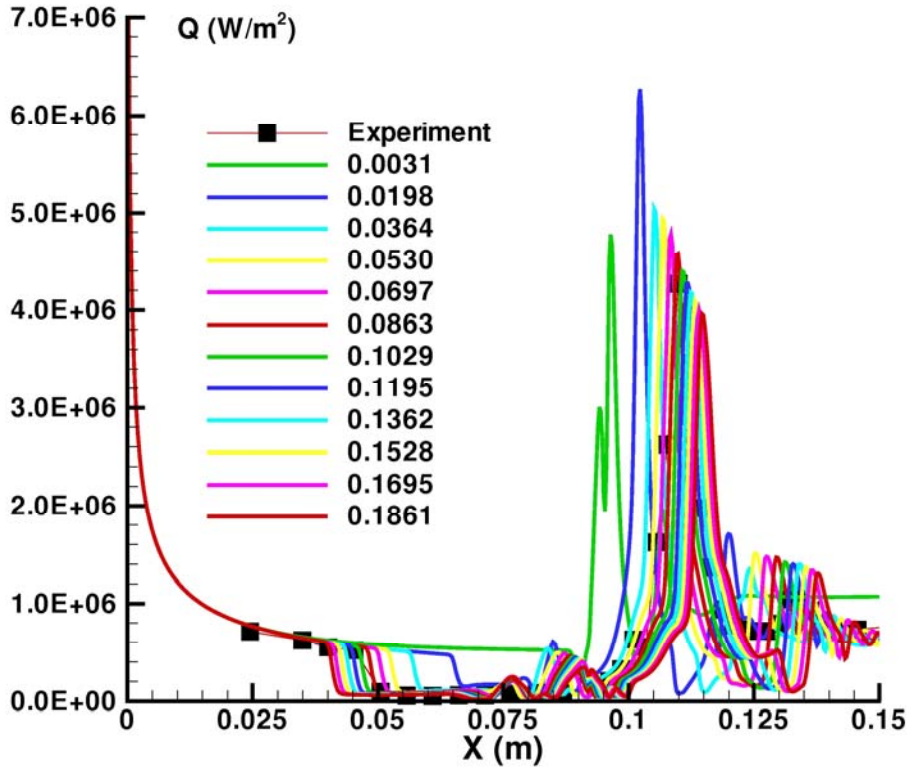

Figure 2-21: q_w for Run 40 (Nompelis).

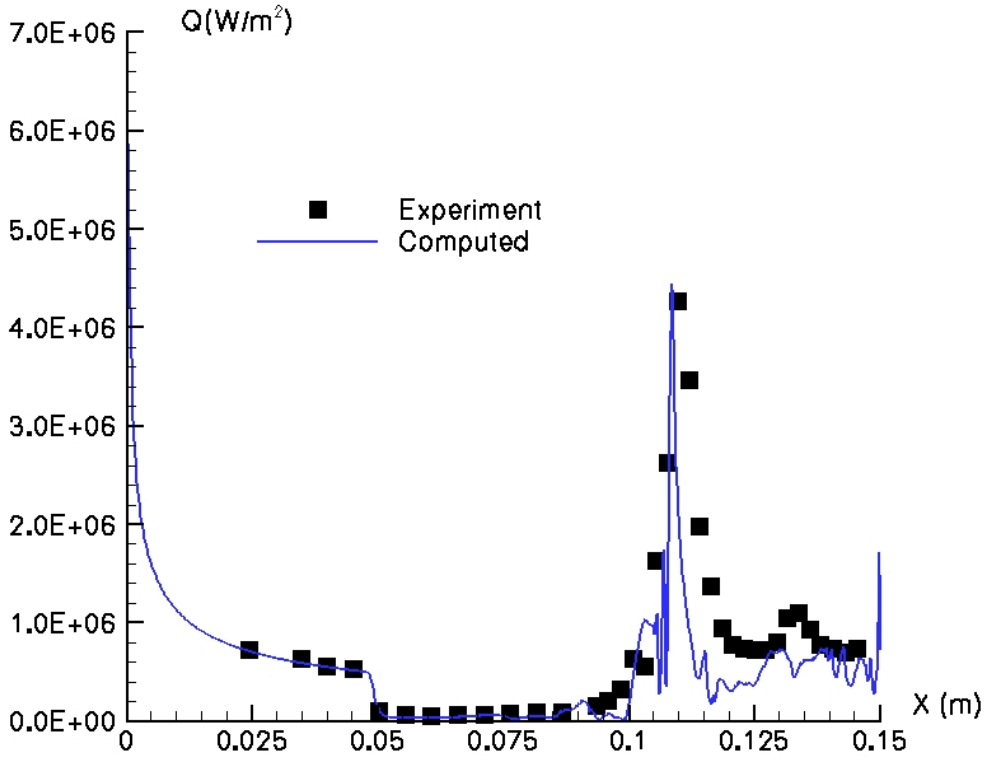

Figure 2-22: q_w for Run 40 (Reimann).

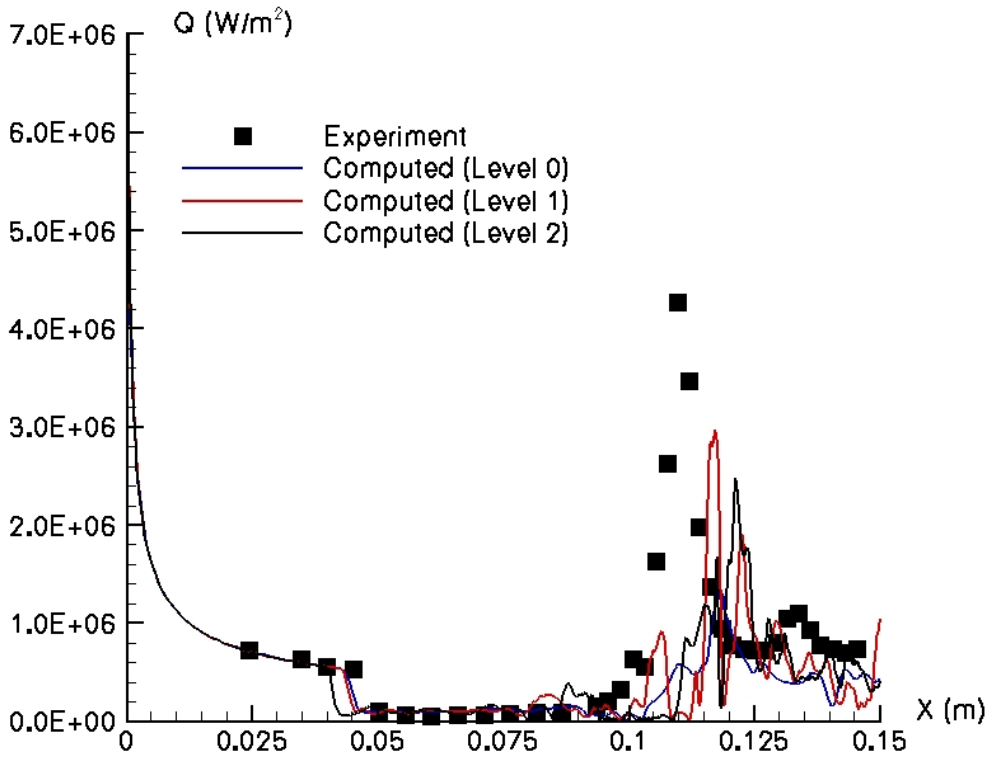

Figure 2-23: q_w for Run 40 (Walpot).

The substantial unsteadiness observed in all computations is in direct contrast to the experimental measurements of surface pressure and heat transfer which indicated a steady flowfield had been achieved. There is no clear explanation for this disagreement between the computations and experiment. It is certainly not attributable to a particular numerical flux algorithm since a variety of different algorithms were used. Also, it is certainly not attributable to a particular grid since several different grid convergence studies were performed by the participants. It may be conjectured that the particular inflow conditions, coupled with the double cone geometry, are close to a configuration of instability and the computations have tended towards this unsteady solution. Further computations and experiments are needed to assess this conjecture.

2.5.2.2 Run 42

The computed surface pressure is compared with experiment in Figure 2-24 to Figure 2-29. All participants observed that the computed flowfield achieved steady state. The location of upstream propagation of the surface pressure (x = 0.050 m) is accurately predicted by the fine grid solution of Gaitonde (Figure 2-24) and the computation of Drikakis et al. using a 5th order WENO scheme (Figure 2-26). All other solutions predict a pressure rise downstream of the experimental location. The plateau pressure associated with separation region (x = 0.05 m to 0.10 m) is accurately predicted by all participants. All computations accurately predict the location of the beginning of the second pressure rise. It is, of course, not necessarily evident that the peak experimental pressure measurement corresponds to the peak surface pressure since the pressure gradient is very large and the surface pressure transducer has finite size. Therefore, it is only possible to assess whether or not the computed peak surface pressure equals or exceeds the experimental value, since an under-prediction of peak surface pressure would indicate a shortcoming in the computation, while a peak computed surface pressure exceeding the peak measured surface pressure may in fact be accurate. Some discrepancies between computations and experiment in the expansion region (x = 0.115 m to 0.125 m) are evident. The computed secondary plateau pressure (x > 0.130 m) appears accurately predicted in all cases.

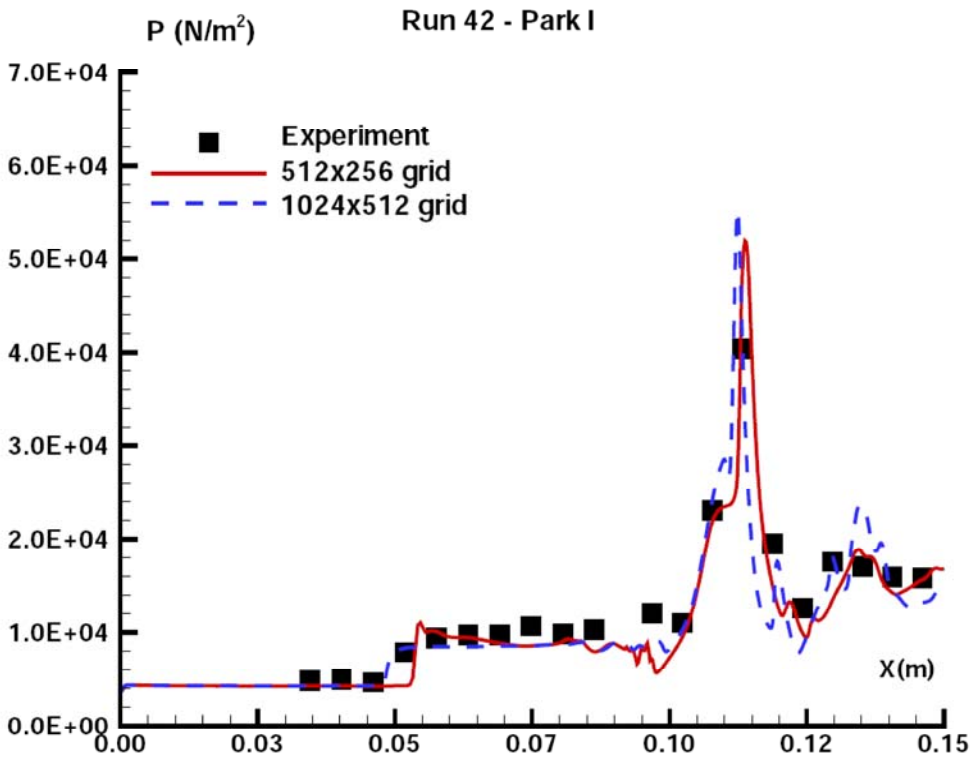

Figure 2-24: p_w for Run 42 (Gaitonde).

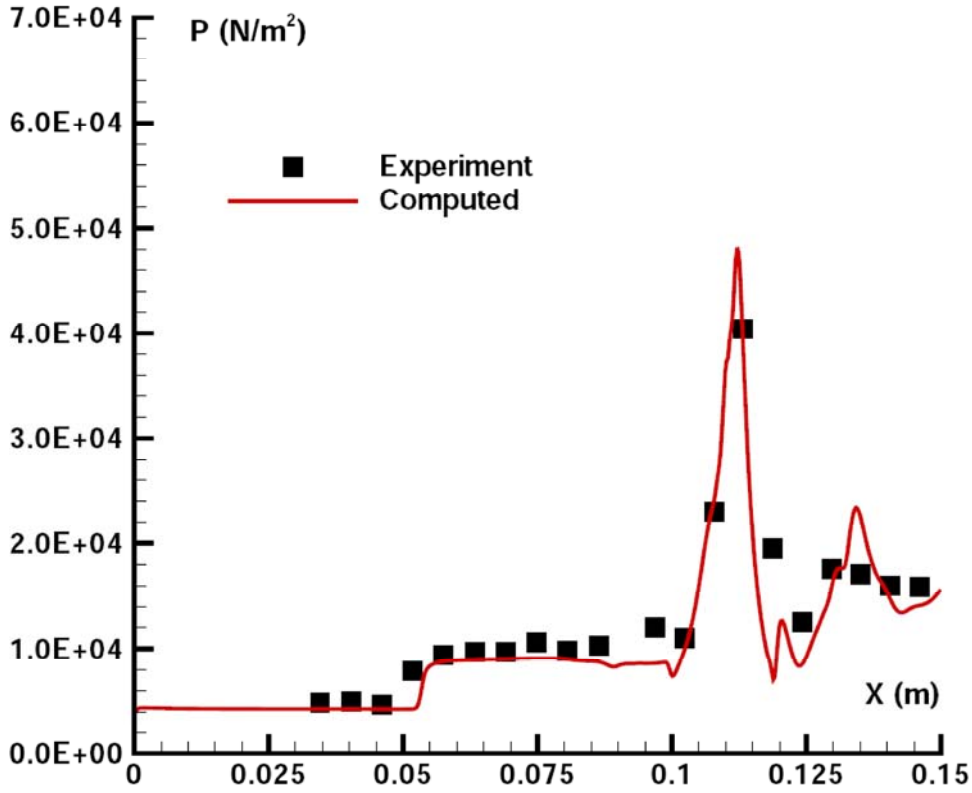

Figure 2-25: p_w for Run 42 (Lani).

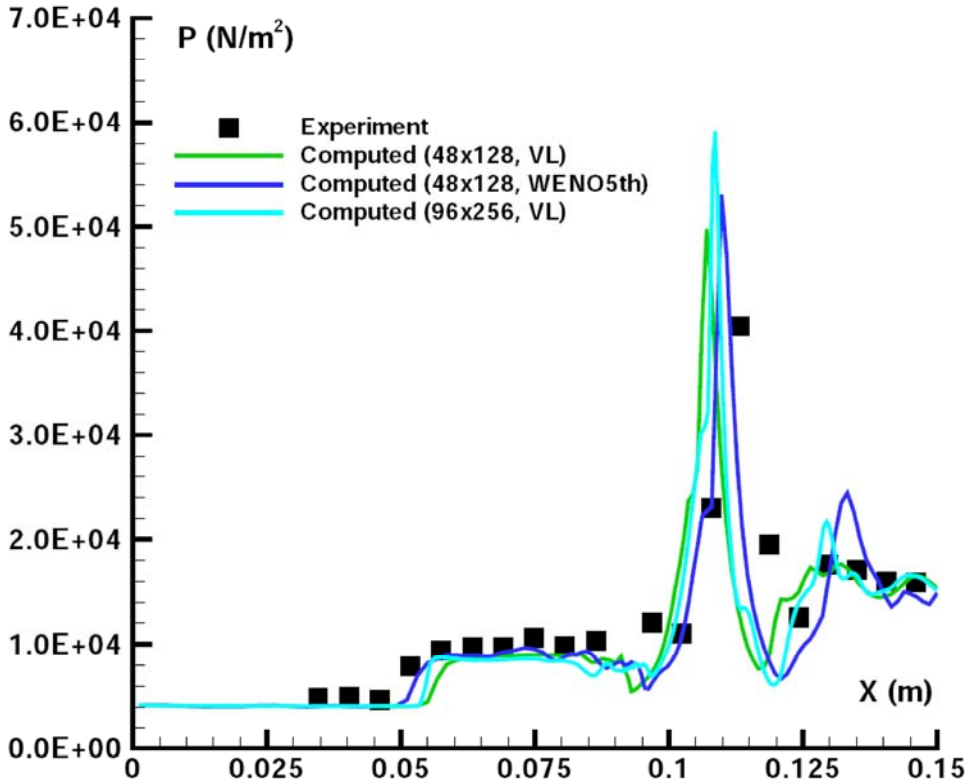

Figure 2-26: p_w for Run 42 (Drikakis et al.).

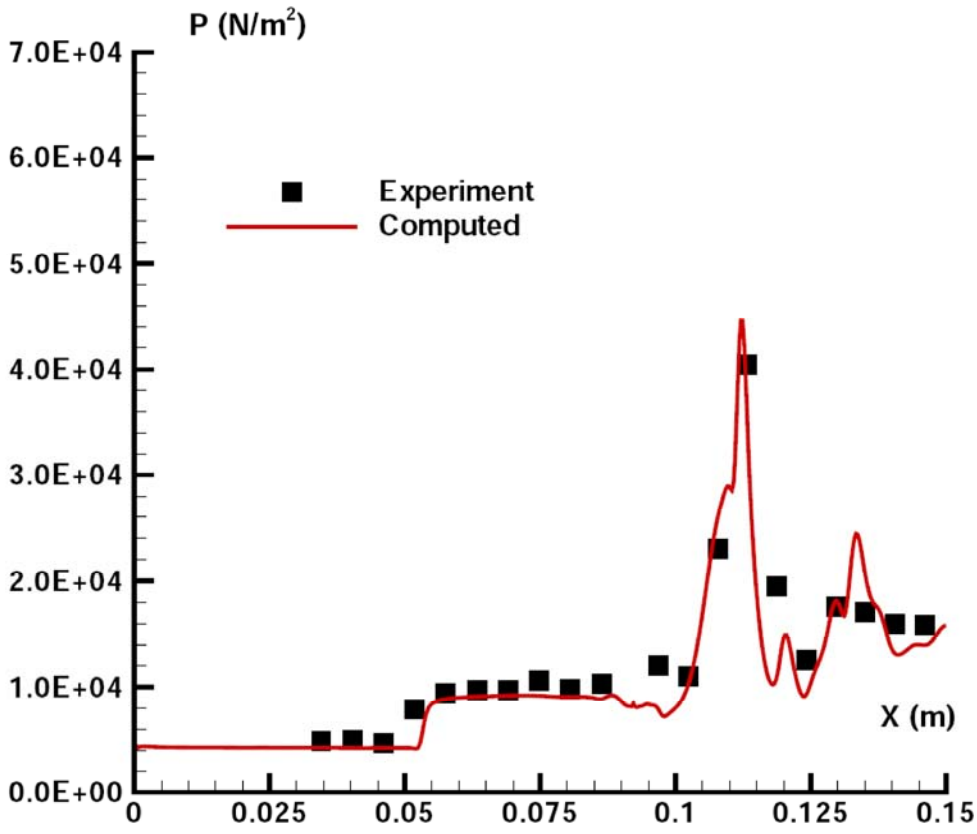

Figure 2-27: p_w for Run 42 (Nompelis).

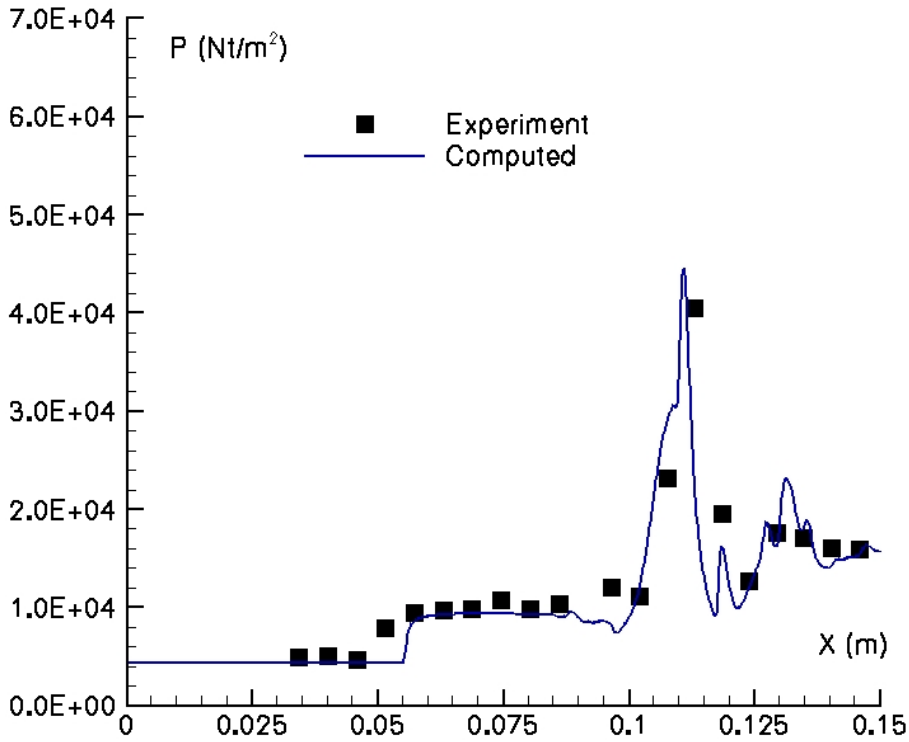

Figure 2-28: p_w for Run 42 (Reimann).

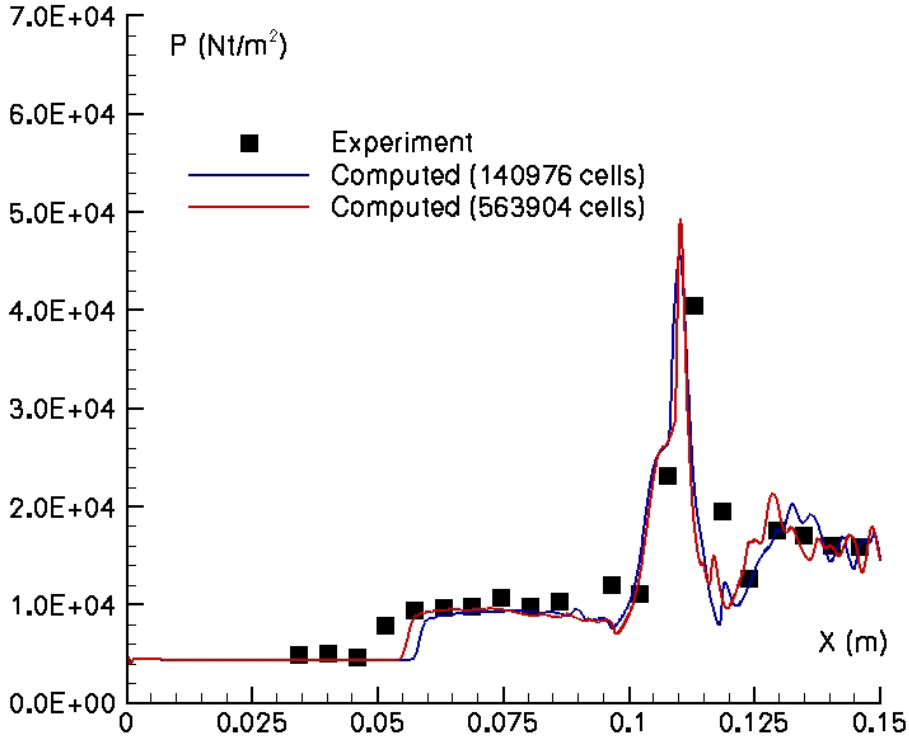

Figure 2-29: p_w for Run 42 (Walpot).

The computed surface heat transfer is compared with experiment in Figure 2-30 to Figure 2-35. The heat transfer upstream of the separation at x = 0.055 m is accurately predicted by all participants. The refined grid (1024 x 512) computation by Gaitonde (Figure 2-30) and the computation of Drikakis et al. using a 5th order WENO scheme (Figure 2-32) show separation at x = 0.050 m while all other solutions show separation at the experimental position (for the finer grid in Figure 2-35). This observation is interesting since these are the two solutions which more closely match the experimental pressure distribution as discussed above. All computations show good agreement with the low level of heat transfer in the separated region, and reasonable agreement with the location of the heat transfer rise at x = 0.105 m. Analogous to the previous discussion regarding peak surface pressure, it is only possible to assess whether or not the computed peak heat transfer equals or exceeds the experimental value. In this regard, the computations of Nompelis (Figure 2-33) and Reimann (Figure 2-34) under-predict the peak experimental heat transfer by 14%, and the fine grid computation by Walpot (Figure 2-35) by 5%.

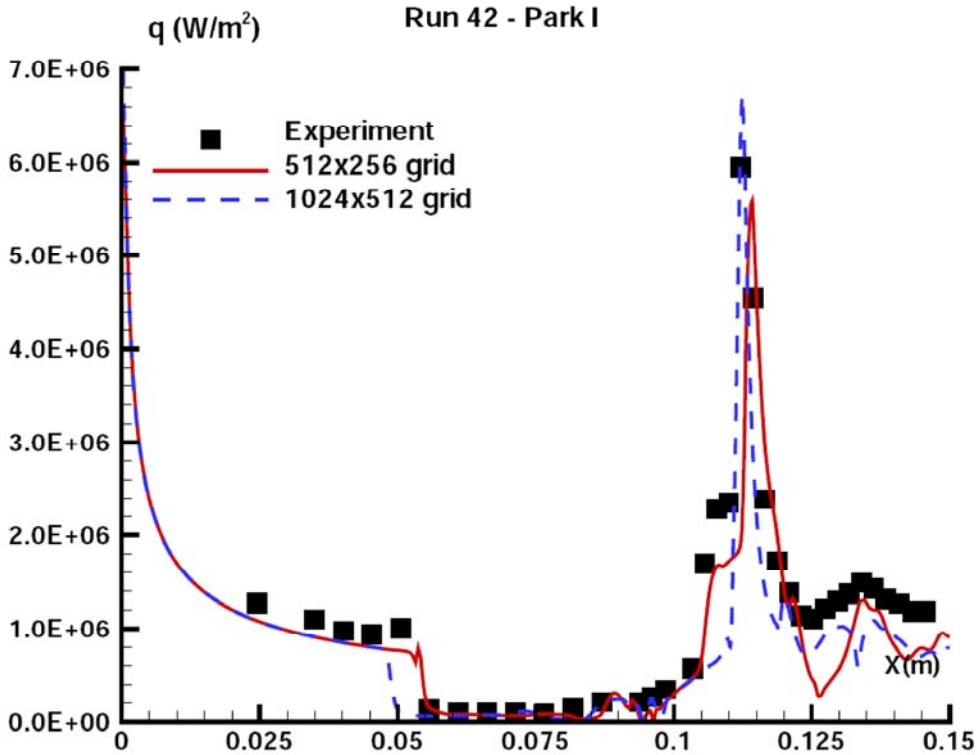

Figure 2-30: q_w for Run 42 (Gaitonde).

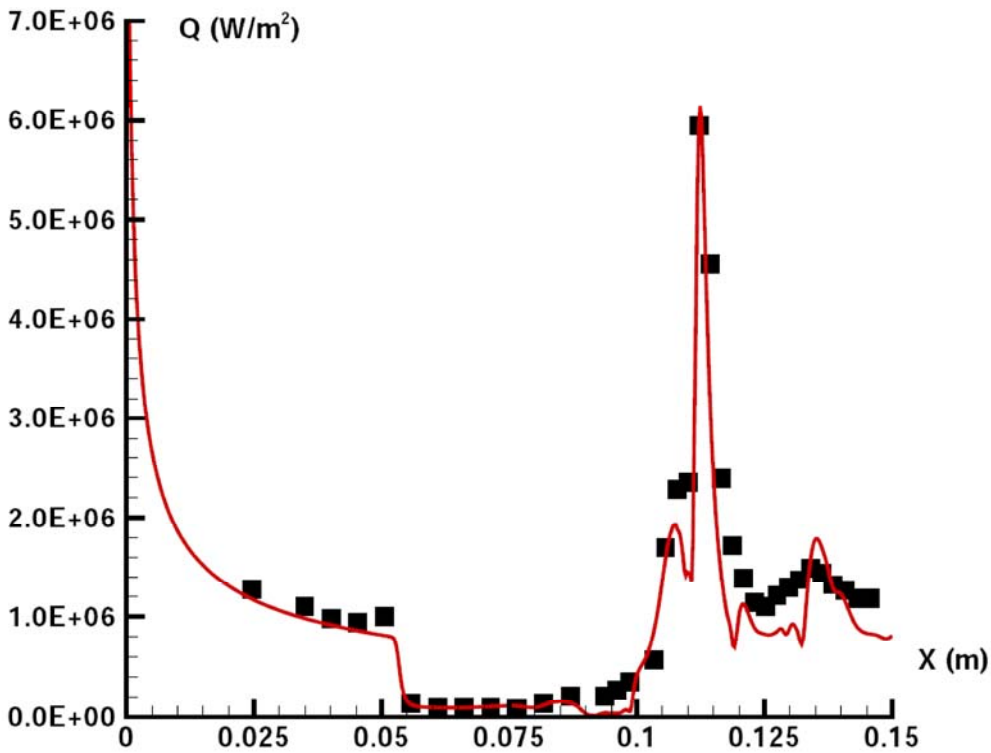

Figure 2-31: q_w for Run 42 (Lani).

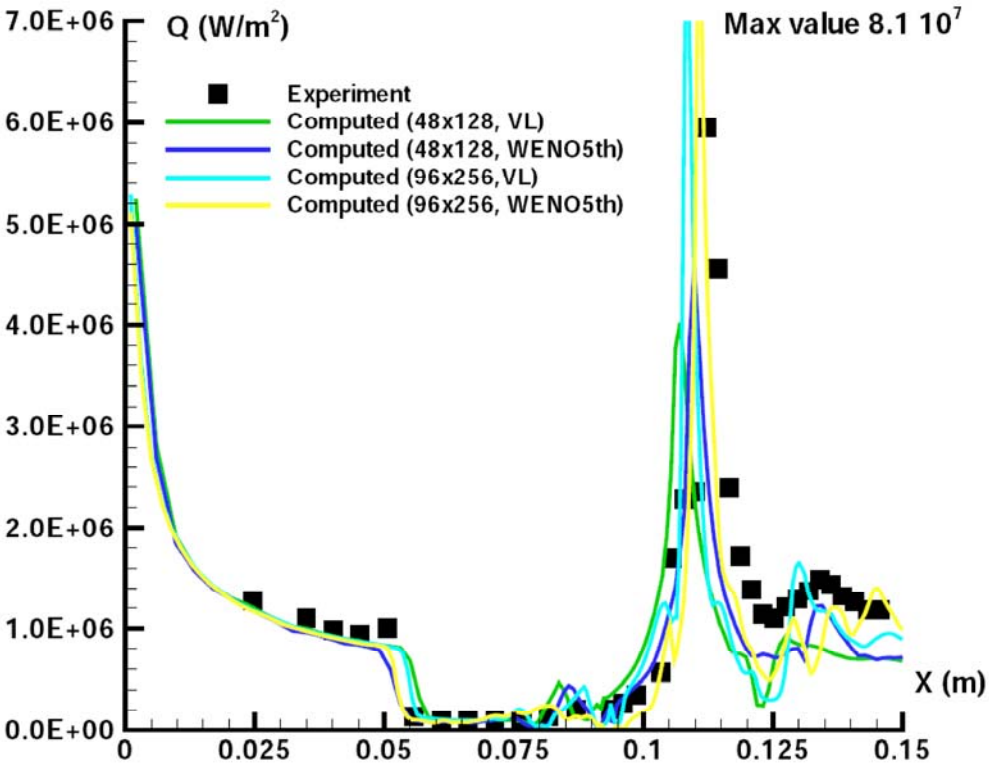

Figure 2-32: q_w for Run 42 (Drikakis et al.).

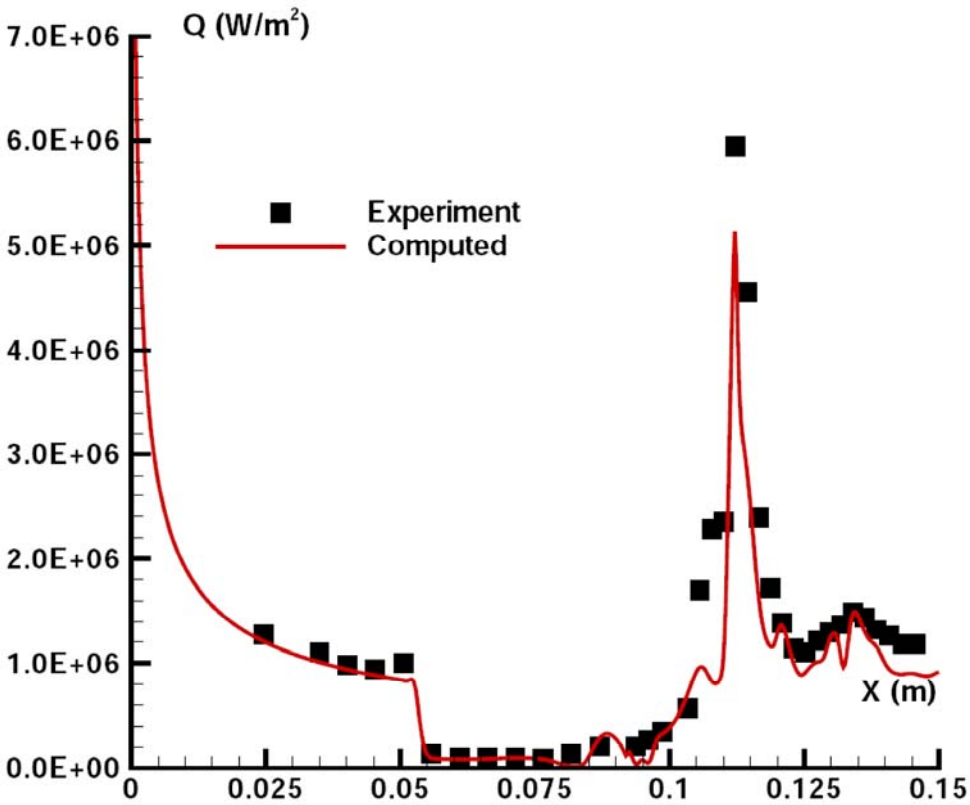

Figure 2-33: q_w for Run 42 (Nompelis).

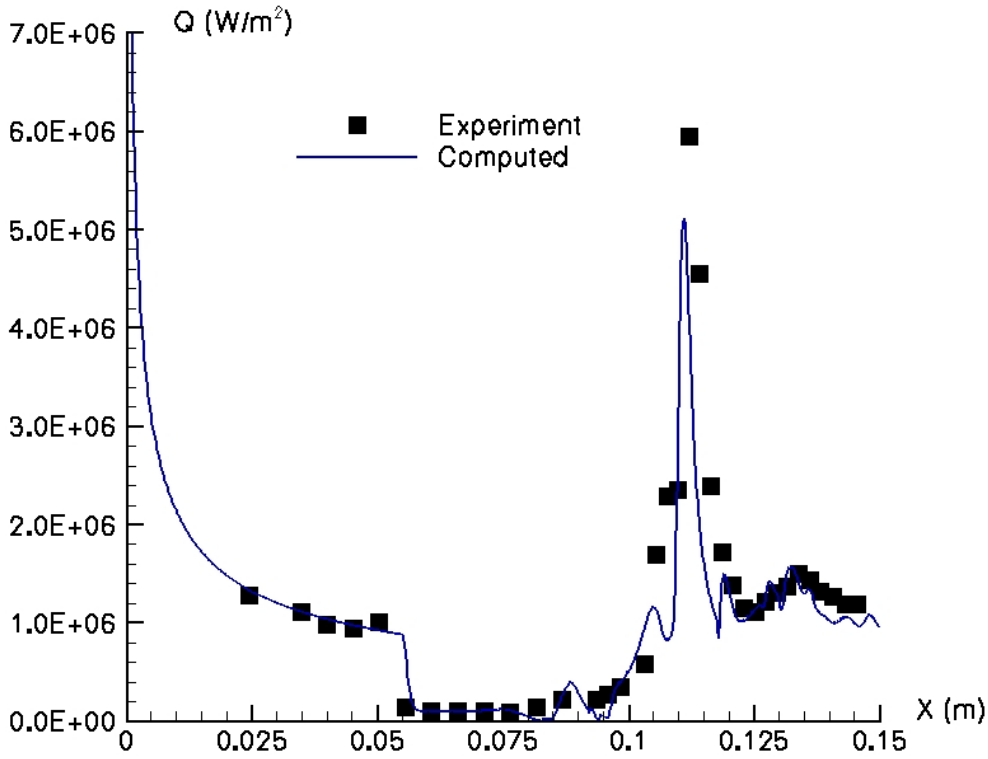

Figure 2-34: q_w for Run 42 (Reimann).

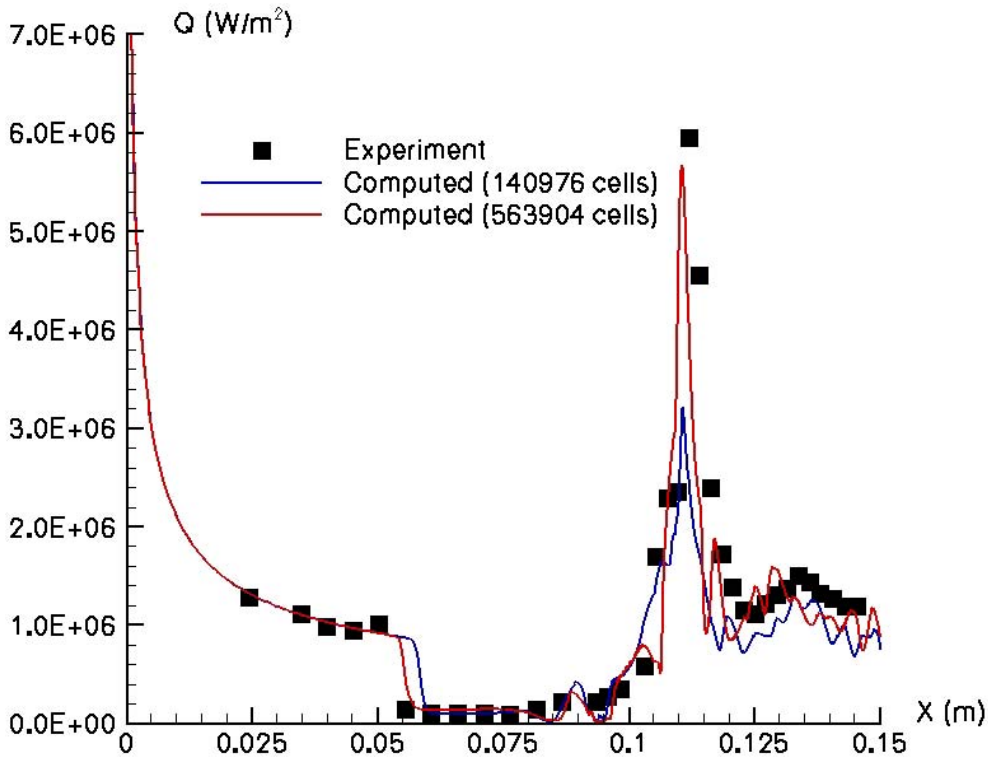

Figure 2-35: q_w for Run 42 (Walpot).

2.5.3 Cylinder

2.5.3.1 Case I

The computed surface pressure is compared with experiment in Figure 2-36 to Figure 2-40. Overall, there is excellent agreement between with experiment for all computations. Virtually identical results are obtained by Nompelis (Figure 2-38) for surface accommodation factor $\gamma = 0$ (non-catalytic) and $\gamma = 1$ (fully catalytic for radicals). All computed flowfields converged to steady state. The computed surface heat transfer is compared with experiment in Figure 2-41 to Figure 2-45. The computed peak heat transfer by Gaitonde (Figure 2-41) under-predicts the experimental peak heat transfer by 25%. The predictions of Lani (Figure 2-42) show closer agreement with experiment, while the fully catalytic predictions of Nompelis (Figure 2-43, $\gamma = 1$) display excellent agreement with experiment. The non-catalytic result of Nompelis, however, under-predicts the peak heat transfer by 25% similar to the results of Gaitonde. The predictions of Walpot (Figure 2-45) also underestimate the peak heat transfer. These results indicate that accurate modeling of surface catalysis is a critical to the prediction of peak heat transfer for this case.

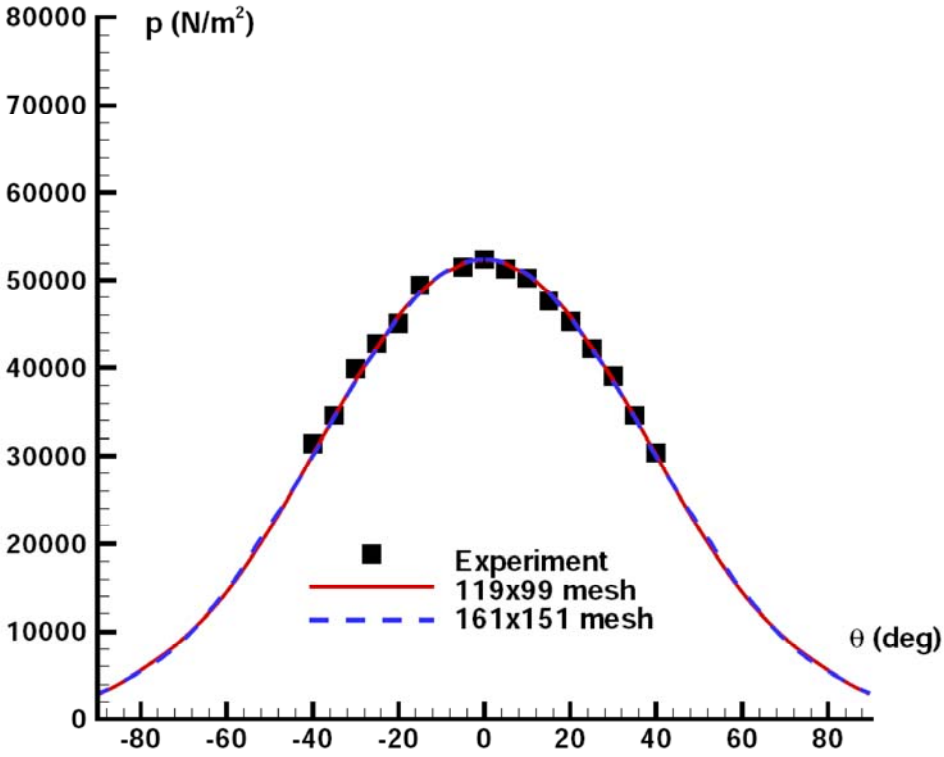

Figure 2-36: p_w for Case I (Gaitonde).

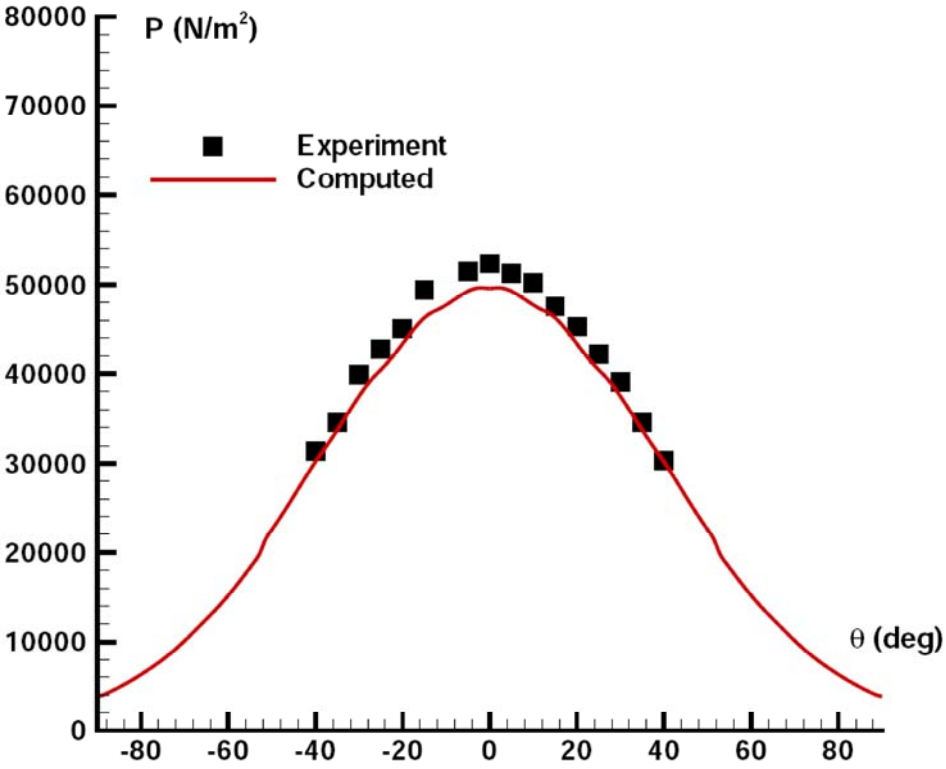

Figure 2-37: p_w for Case I (Lani).

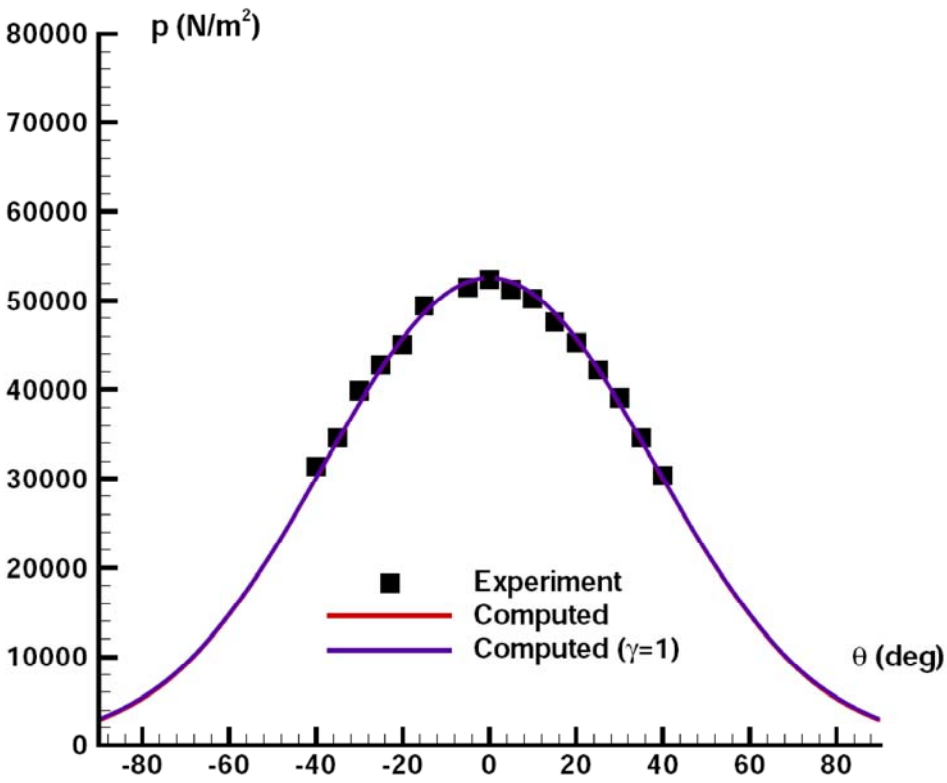

Figure 2-38: p_w for Case I (Nompelis).

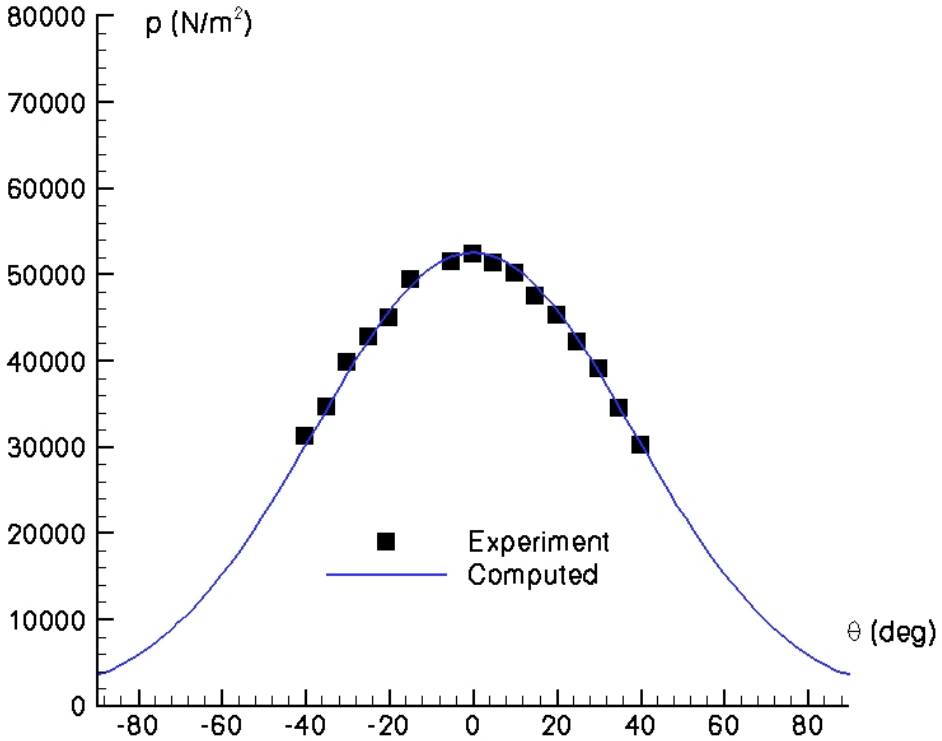

Figure 2-39: p_w for Case I (Reimann).

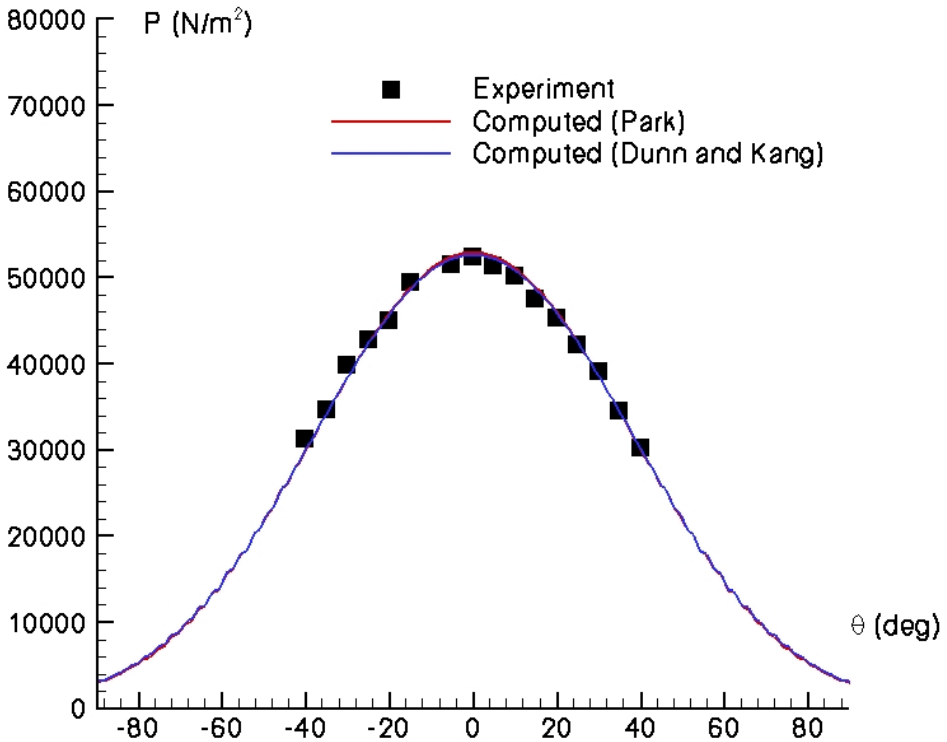

Figure 2-40: p_w for Case I (Walpot).

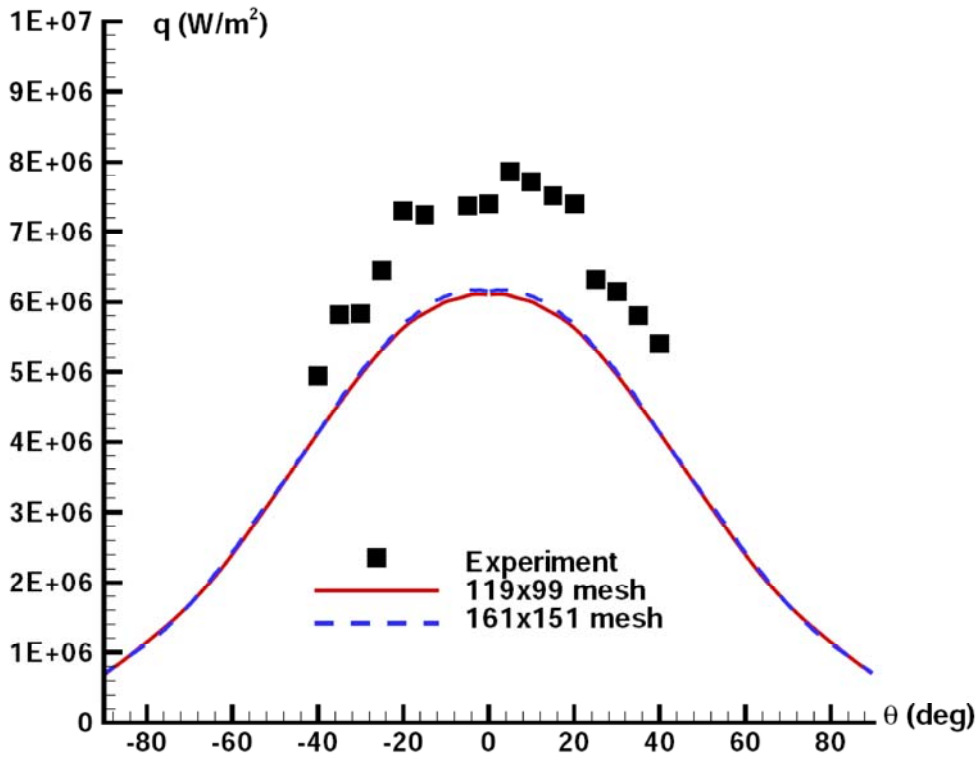

Figure 2-41: q_w for Case I (Gaitonde).

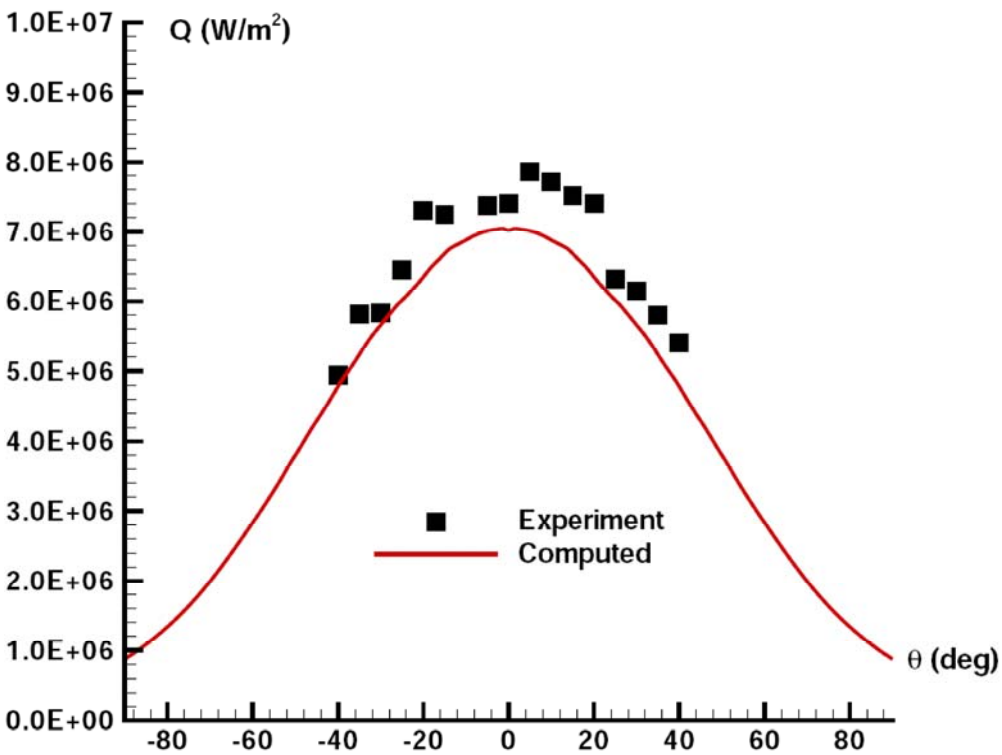

Figure 2-42: q_w for Case I (Lani).

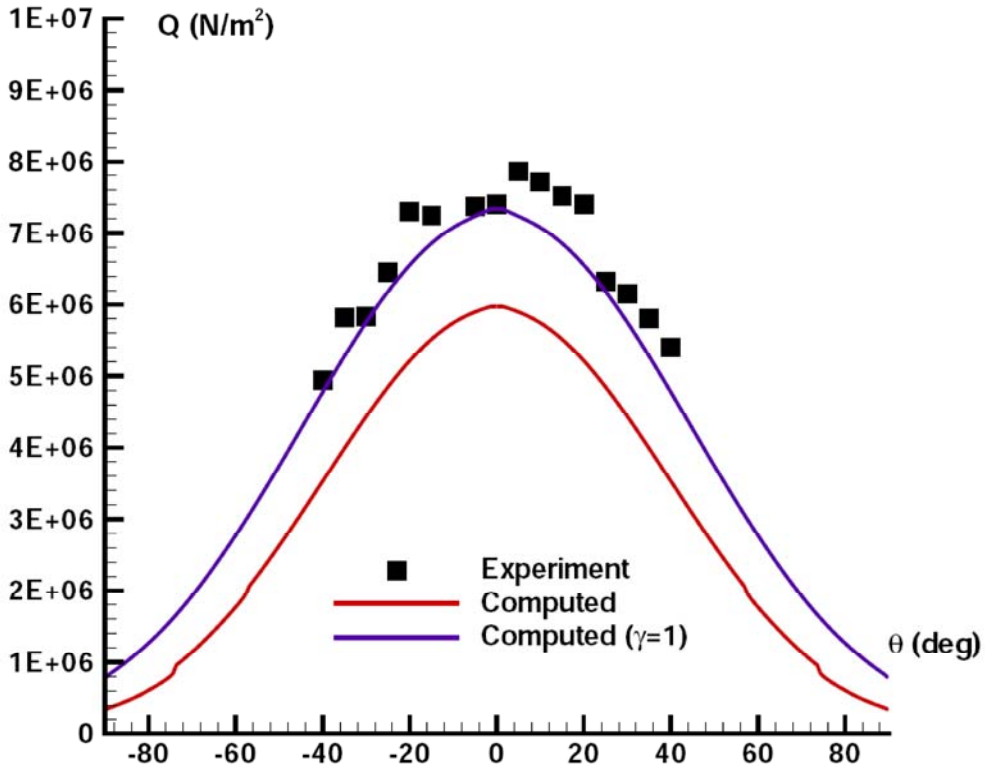

Figure 2-43: q_w for Case I (Nompelis).

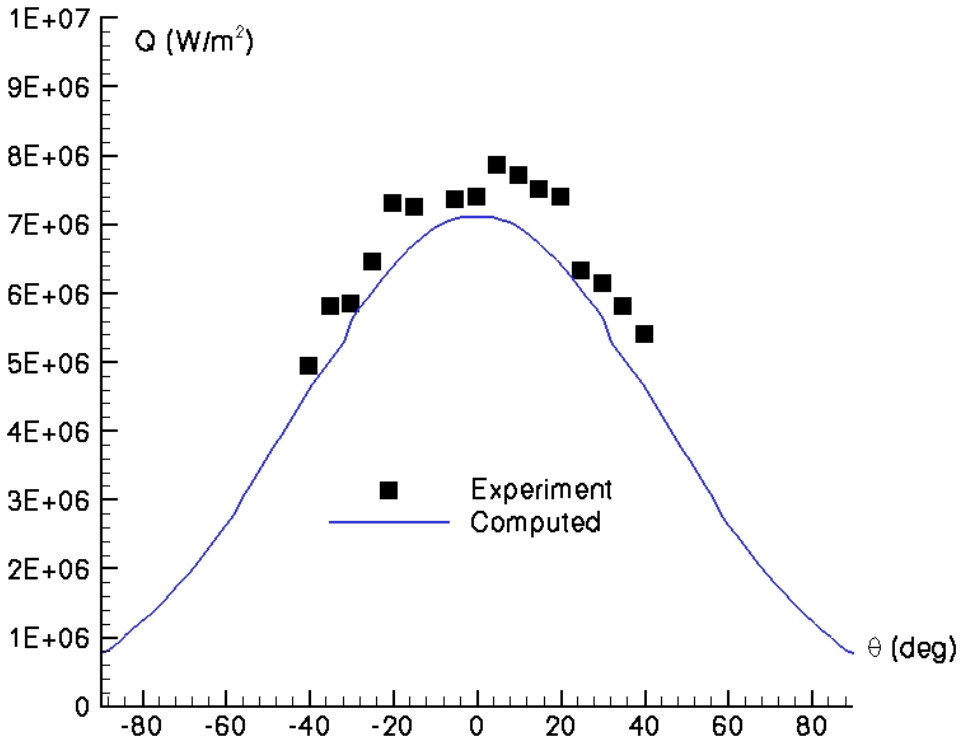

Figure 2-44: q_w for Case I (Reimann).

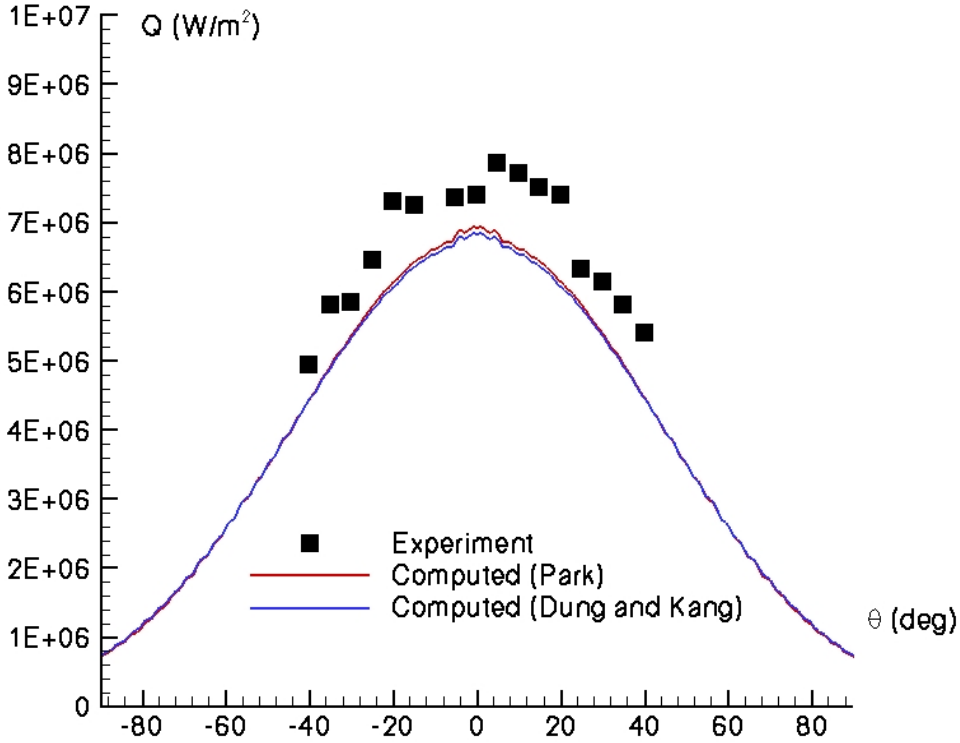

Figure 2-45: q_w for Case I (Walpot).

2.5.3.2 Case III

The computed surface pressure is compared with experiment in Figure 2-46 to Figure 2-50. Overall, there is good agreement with the pressure distribution on the surface for all computations. The predictions of Nompelis (Figure 2-48) for both non-catalytic ($\gamma = 0$) and catalytic ($\gamma = 1$) cases are virtually identical. The computed surface heat transfer is compared with experiment in Figure 2-51 to Figure 2-55. The peak experimental heat transfer is lower than for Case I as expected from the lower freestream total enthalpy in this case (Table 2-2). All predictions are in reasonable agreement with experiment. In particular, the effect of catalycity in the computations of Nompelis (Figure 2-53) are significantly less than in Case I.

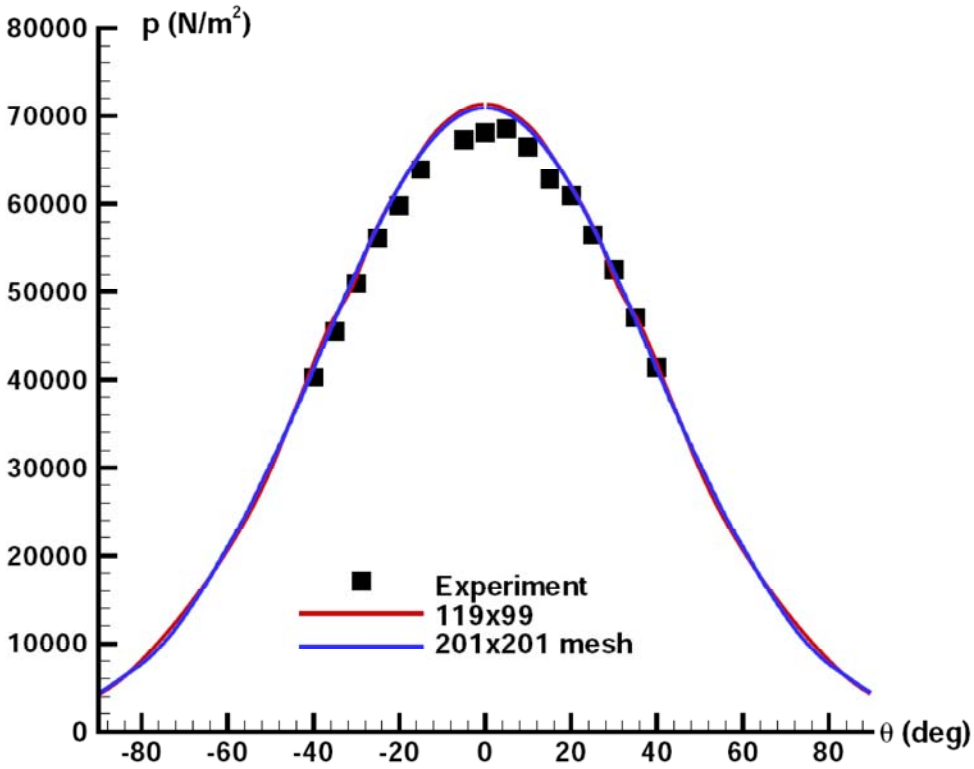

Figure 2-46: p_w for Case III (Gaitonde).

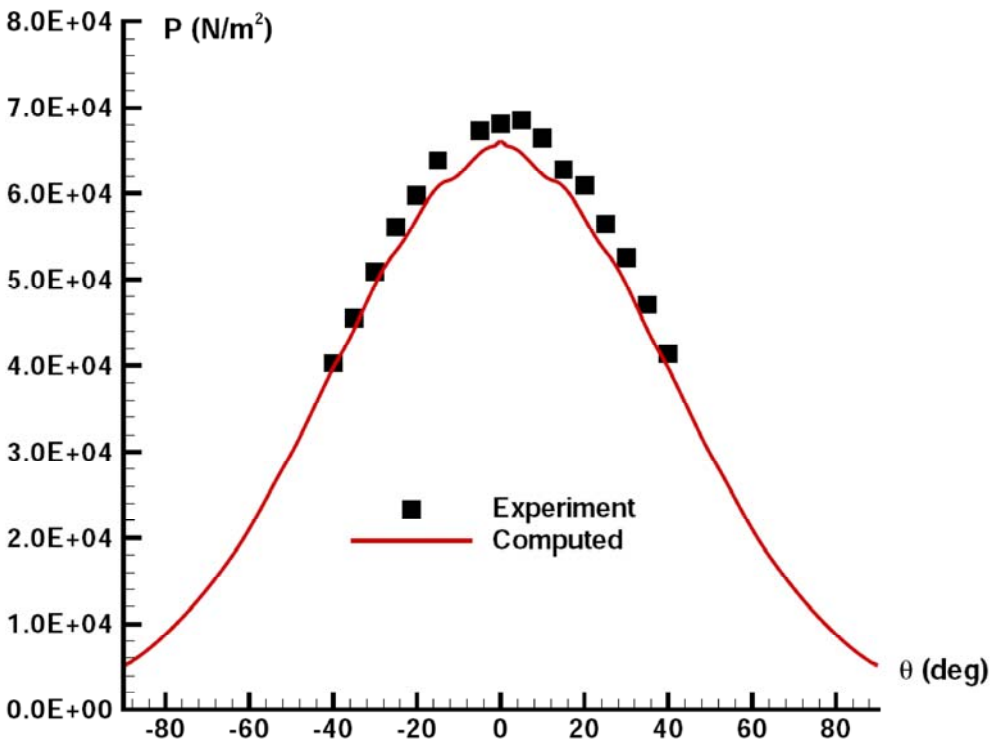

Figure 2-47: p_w for Case III (Lani).

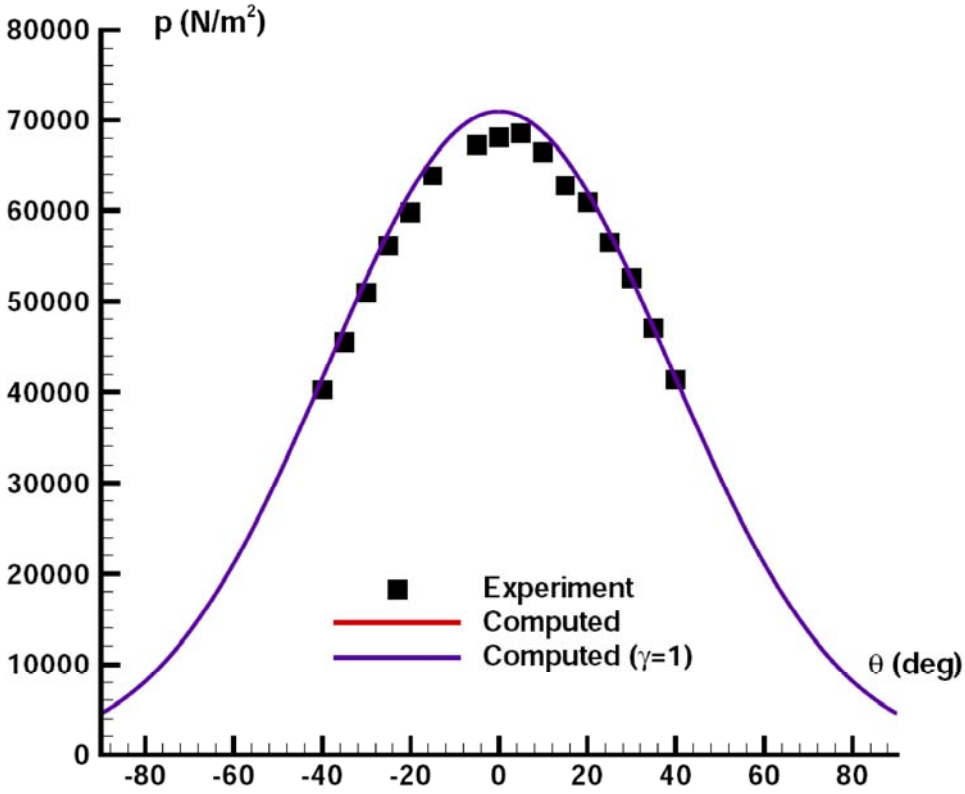

Figure 2-48: p_w for Case III (Nompelis).

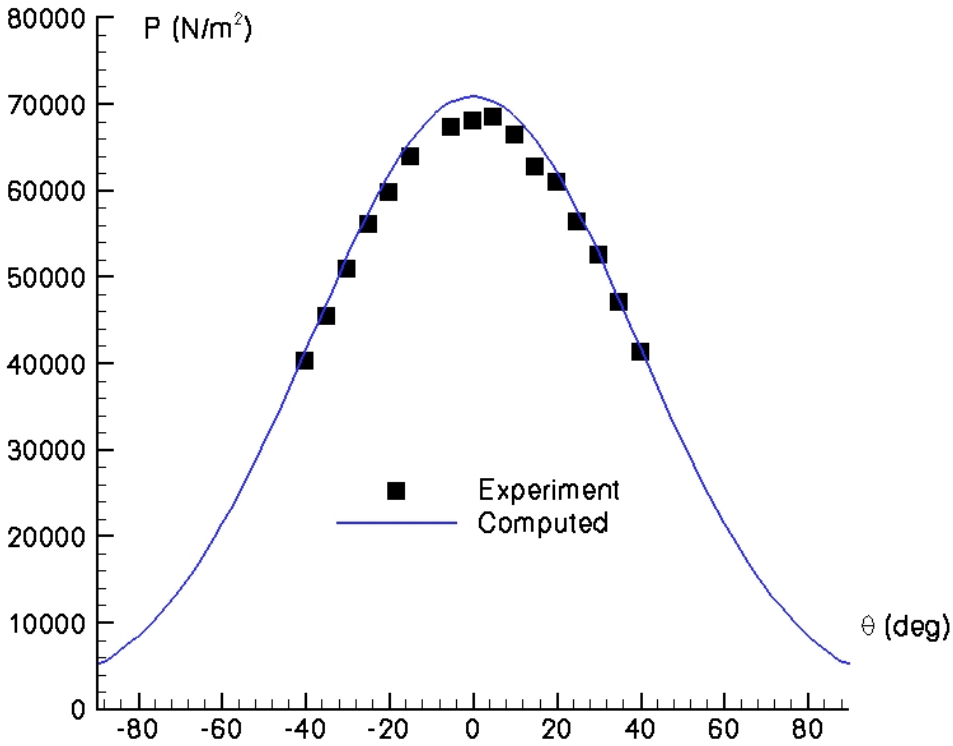

Figure 2-49: p_w for case III (Reimann).

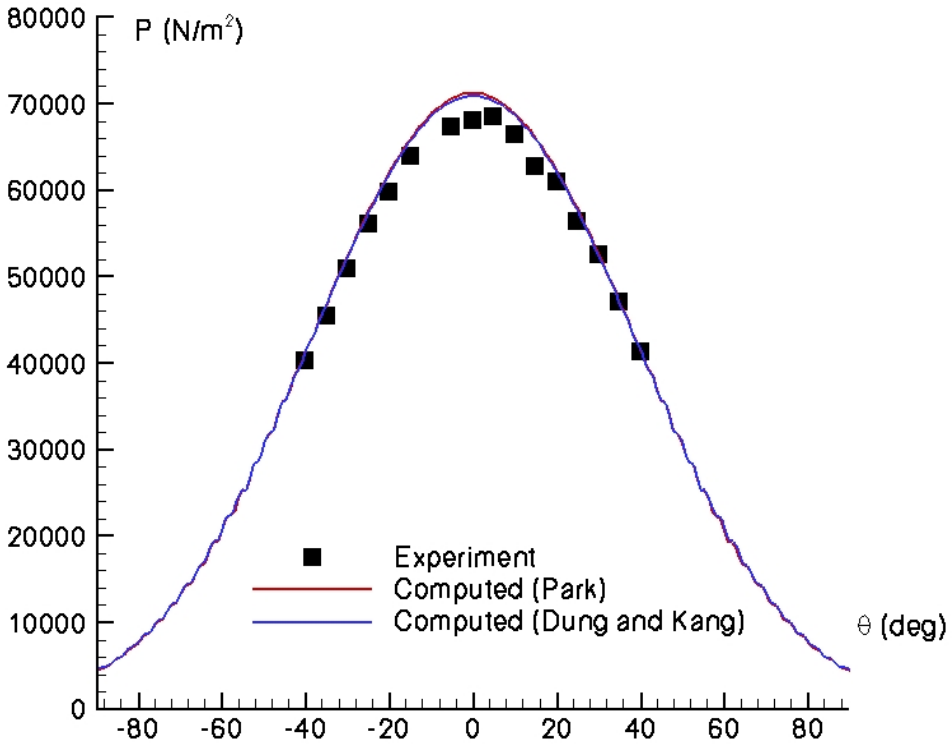

Figure 2-50: p_w for Case III (Walpot).

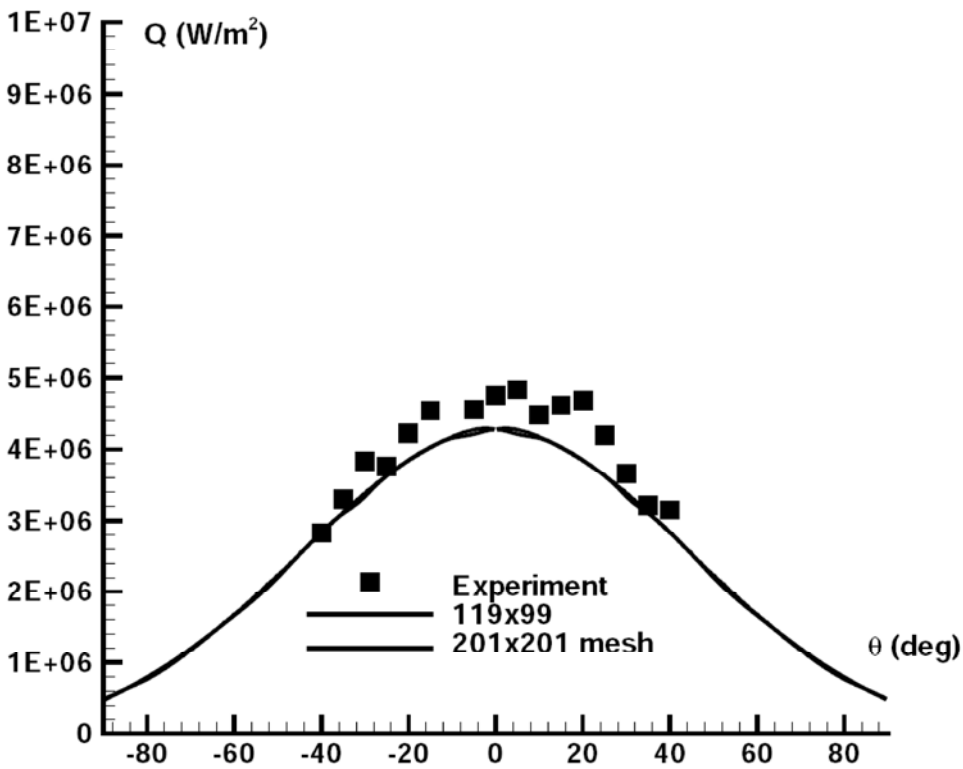

Figure 2-51: q_w for Case III (Gaitonde).

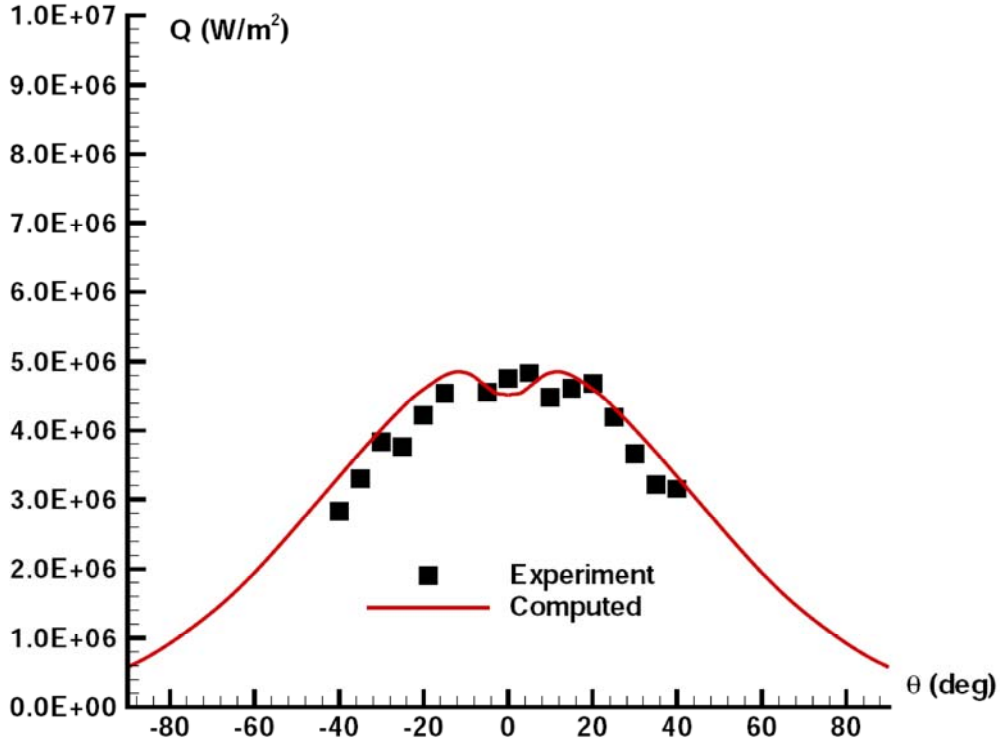

Figure 2-52: q_w for Case III (Lani).

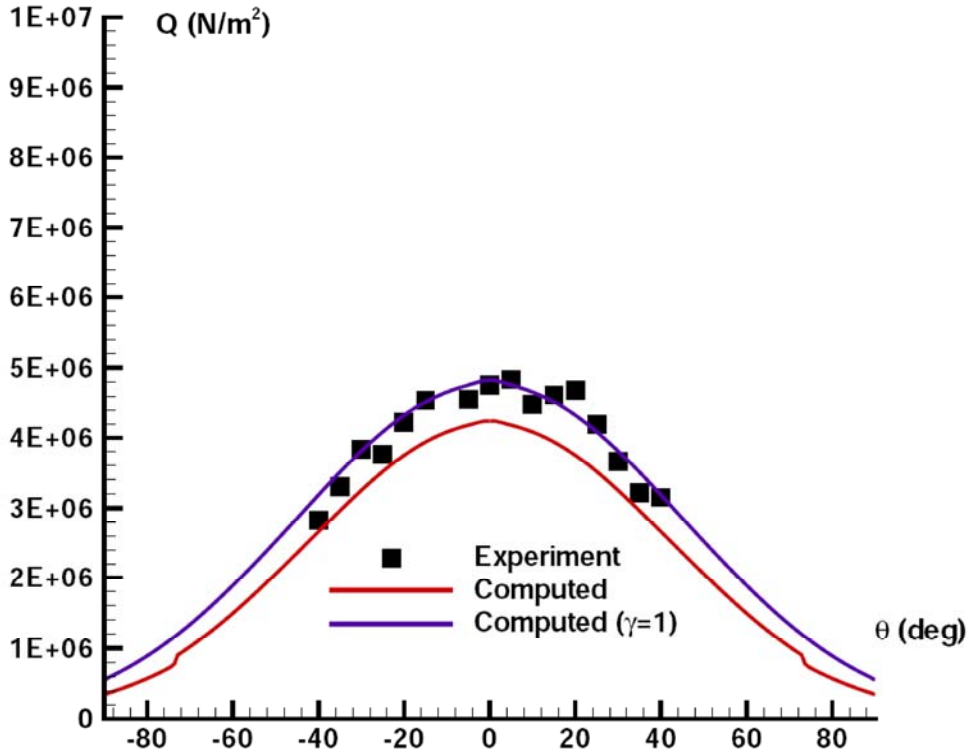

Figure 2-53: q_w for Case III (Nompelis).

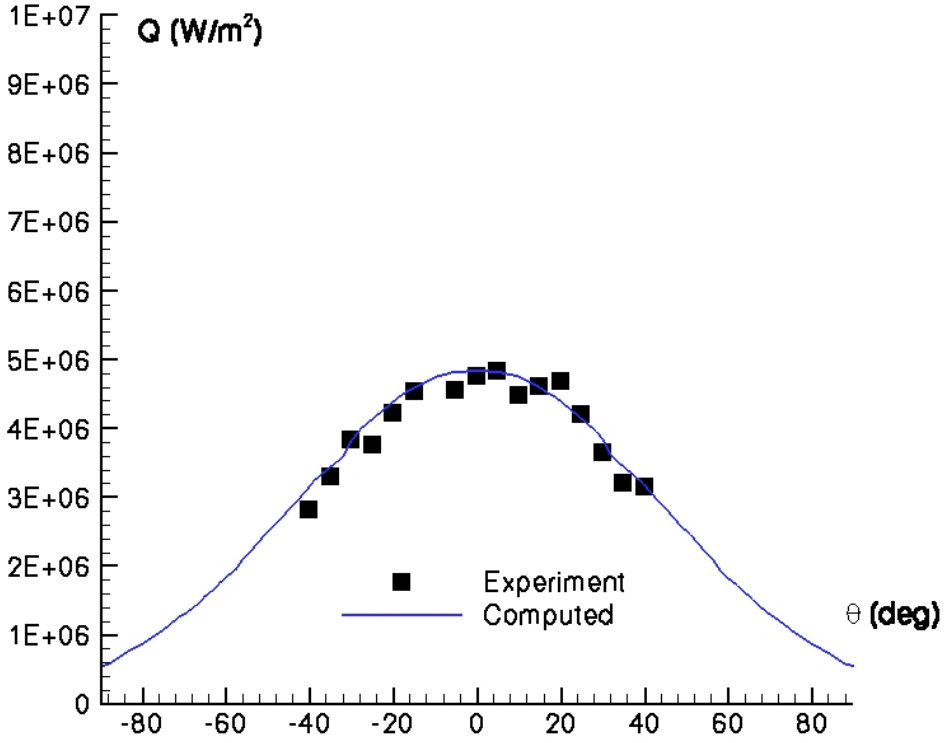

Figure 2-54: q_w for Case III (Reimann).

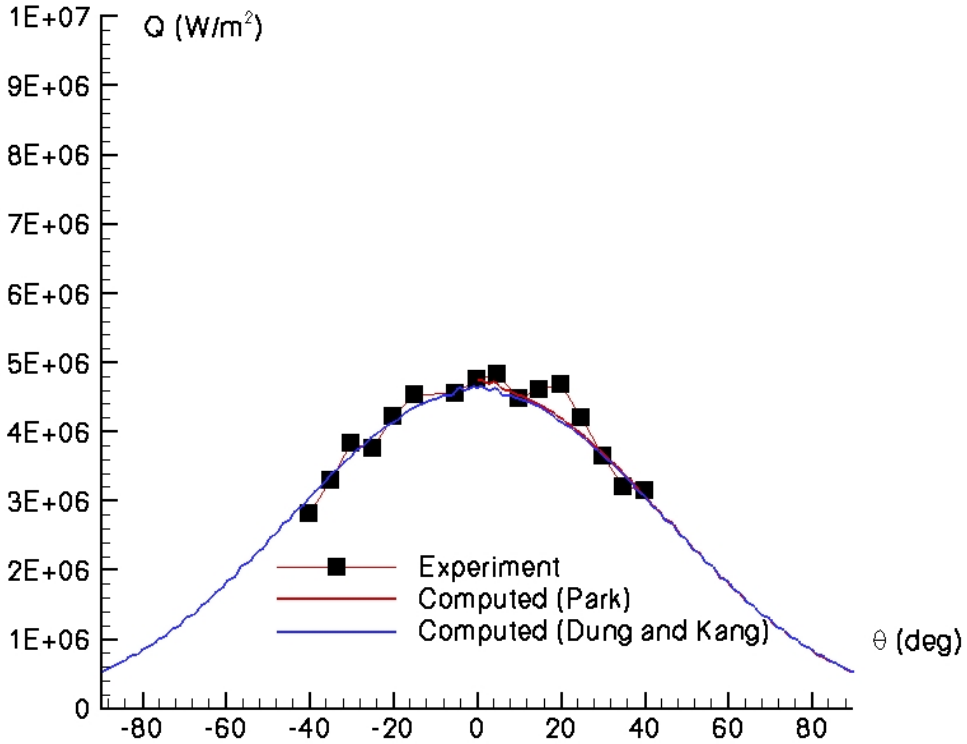

Figure 2-55: q_w for Case III (Walpot).

2.6 CONCLUSIONS

A collaborative effort on assessment of CFD capability for prediction of shock interactions was performed. A matrix of two test configurations (double cone and cylinder) was selected with two separate flow conditions for each configuration. Experimental data for surface pressure and heat transfer was provided for each configuration. Six CFD experts from Europe and the United States performed computations for most or all of the configurations and the results are compared with the experimental data. For the double cone configuration, a surprising result was observed for the first test case (Run 40). The experiment indicated that a steady flowfield had been achieved, while all computations indicated that a steady state solution had not been reached. This is a critically important result which requires further detailed investigation. For the second test case (Run 42), generally good agreement was obtained for surface pressure and heat transfer. For the cylinder configuration, close agreement was achieved for the surface pressure for both test conditions. However, the computed peak heat transfer was typically under-predicted by up to 25% for the higher freestream enthalpy configuration (Case I) in the absence of catalytic effects in the surface boundary conditions. This emphasizes the need for further research in modeling gas-surface interactions at high freestream enthalpy conditions. The computed heat transfer was in reasonable agreement for the lower freestream enthalpy case (Case III).

2.7 REFERENCES

[1] Barth, T., "Aspects of Unstructured Grids and Finite Volume Solvers for the Euler and Navier-Stokes Equations", Von Karman Institute for Fluid Dynamics, Lecture Series No. 1994-05, 1994.

[2] Blottner, F., Johnson, M. and Ellis, M., "Chemically Reacting Viscous Flow Program for Multicomponent Gas Mixtures", Technical Report SC-RR-70-754, Sandia National Laboratories, Albuquerque, NM, USA, 1971.

[3] Candler, G., "Hypersonic Nozzle Analysis Using an Excluded Volume Equation of State", AIAA Paper No. 2005-5202, American Institute of Aeronautics and Astronautics, January 2005.

[4] Csik, A., Ricchiuto, M. and Deconinck, H., "A Conservative Formulation of the Multidimensional Upwind Residual Distribution Schemes for General Nonlinear Conservation Laws", *Journal of Computational Physics*, Vol. 179, No. 2, pp. 286-312, 2002.

[5] Dobes, J. and Deconinck, H., "A Shock Sensor-Based Second-Order Blended (Bx) Upwind Residual Distribution Scheme for Steady and Unsteady Compressible Flow", In *Hyperbolic Problems: Theory, Numerics, Applications*, 978-3-540-75711-5 (print), 978-3-540-75712-2 (online), pp. 465-473, Springer, Berlin, 2008.

[6] Drikakis, D., "Advances in Turbulent Flow Computations Using High-Resolution Methods", *Progress in Aerospace Sciences*, Vol. 39, pp. 405-424, 2003.

[7] Drikakis, D., Hahn, M., Mosedale, A. and Thorber, B., "Large Eddy Simulation Using High Resolution and High Order Methods", *Philosophical Transactions Royal Society A*, 367, pp. 2985-2997, 2009.

[8] Drikakis, D. and Tsangaris, S., "An Implicit Flux-Averaging Scheme for the Euler Equations for Real Gases", *International Journal for Numerical Methods in Fluids*, Vol. 12, pp. 711-726, 1991.

[9] Druguet, M.-C., Candler, G. and Nompelis, I., "Effect of Numerics on Navier-Stokes Computations of Hypersonic Double-Cone Flows", *AIAA Journal*, Vol. 43, No. 3, pp. 616-623, March 2005.

[10] Gupta, R., Yos, J., Thompson, R. and Lee, K.-P., "A Review of Reaction Rates and Thermodynamic and Transport Properties for an Eleven-Species Model for chemical and Thermal Nonequilibrium Calculations to 30,000 K", Reference Publication No. 1232, NASA, 1990.

[11] Karl, S., Martinez-Schramm, J. and Hannemann, K., "High Enthalpy Cylinder Flow in HEG: A Basis for CFD Validation", AIAA Paper No. 2003-4252, American Institute of Aeronautics and Astronautics, June 2003.

[12] Knight, D. and Degrez, G., "Shock Wave Boundary Layer Interactions in High Mach Number Flows: A Critical Survey of Current Numerical Predictions", AGARD Report 319, AGARD, pp. 1-1 to 1-35, December 1998.

[13] Knight, D., RTO WG 10: "Test Cases for CFD Validation of Hypersonic Flight", AIAA Paper No. 2002-0433, American Institute of Aeronautics and Astronautics, January 2002.

[14] Lani, A., Quintino, T., Kimpe, D., Deconinck, H., Vandewalle, S. and Poedts, S., "The COOLFluiD Framework: Design Solutions for High Performance Object Oriented Scientific Computing Software", In *Computational Science ICCS 2005*, Sloot, P., Sunderan, V., van Albada, G. and Dongarra, J. (Eds.), Vol. 1 of LNCS 3514, pp. 28-286, Atlanta, GA, USA, Springer, May 2005.

[15] Lani, A., Quintino, T., Kimpe, D., Deconinck, H., Vandewalle, S. and Poedts, S., "Reusable Object Oriented Solutions for Numerical Simulation of PDEs in a High Performance Environment", *Scientific Programming*, Special Edition on POOSC 2005, Vol. 14, No. 2, pp. 111-139, 2006.

[16] Lani, A., "An Object Oriented and High Performance Platform for Aerothermodynamics Simulation", PhD Thesis, Université Libre de Bruxelles, 2008.

[17] Liou, M., "A Sequel to AUSM: AUSM+", *Journal of Computational Physics*, Vol. 129, No. 2, pp. 364-382, December 1996.

[18] MacCormack, R. and Candler, G., "The Solution of the Navier-Stokes Equations Using Gauss-Seidel Line Relaxation", *Computers and Fluids*, Vol. 17, No. 1, pp. 135-150, 1989.

[19] Magin, T. and Degrez, G., "Transport Algorithms for Partially Ionized Unmagnetized Plasmas", *Journal of Computational Physics*, Vol. 198, pp. 424-449, 2004.

[20] Millikan, R. and White, D., "Systematics of Vibrational Relaxation", *Journal of Chemical Physics*, Vol. 39, pp. 3209-3213, 1953.

[21] Morrison, J., "Flux-difference Split Scheme for Turbulent Transport Equations", AIAA Paper No. 1990-5251, American Institute of Aeronautics and Astronautics, October 1990.

[22] Nompelis, I., "Computational Study of Hypersonic Double-Cone Experiments for Code Validation", PhD Thesis, Department of Aerospace Engineering and Mechanics, University of Minnesota, MN, USA, May 2004.

[23] Panesi, M., "Physical Models for Nonequilibrium Plasma Flow Simulations at High Speed Re-entry Conditions", PhD Thesis, Universita di Pisa, Von Karman Institute of Fluid Dynamics, 2008.

[24] Park, C., "Non-equilibrium Hypersonic Aerothermodynamics", Wiley-Interscience, New York, NY, USA, 1990.

[25] Park, C., "Review of Chemical-Kinetic Problems of Future NASA mission, I: Earth Entries", *Journal of Thermophysics and Heat Transfer*, Vol. 7, pp. 385-398, July-September 1993.

[26] Roe, P., "Approximate Riemann Solvers, Parametric Vectors and Difference Schemes", *Journal of Computational Physics*, Vol. 43, pp. 357-372, 1981.

[27] Quintino, T., "A Component Environment for High-Performance Scientific Computing: Design and Implementation", PhD Thesis, Katholieke Universiteit Leuven, 2008.

[28] Schwamborn, D., Gerhold, T. and Heinrich, R., "The DLR TAU Code: Recent Applications in Research and Industry", In *ECCOMASS CFD 2006,* Wesseling, P. et al. (Eds.), TU Delft, Netherlands, 2006.

[29] Venkatakrishnan, V., "Convergence to Steady State Solutions of the Euler Equations on Unstructured Grids with Limiters", *Journal of Computational Physics*, Vol. 118, pp. 120-130, 1995.

[30] Vincenti, W. and Kruger, C., "Introduction to Physical Gas Dynamics", Krieger Publishing Company, Malabar, FL, USA, 1965.

[31] Wright, M., Bose, D. and Candler, G., "A Data-Parallel Line Relaxation Method for the Navier-Stokes Equations", *AIAA Journal*, Vol. 36, No. 9, pp. 1603-1609, September 1998.